



# TECHNICAL MEMORANDUM

X-664

THE EFFECT OF BOW-SHOCK-FLARE-SHOCK INTERACTION ON  
THE STATIC LONGITUDINAL STABILITY OF FLARE-STABILIZED BODIES  
AT HYPERSONIC SPEEDS

By Paul E. Fitzgerald, Jr.

Langley Research Center  
Langley Air Force Base, Va.

REPRODUCED BY  
NATIONAL TECHNICAL  
INFORMATION SERVICE  
U.S. DEPARTMENT OF COMMERCE  
SPRINGFIELD, VA. 22161

(NASA-TM-X-664) - THE EFFECT OF  
BOW-SHOCK-FLARE-SHOCK INTERACTION ON THE  
STATIC LONGITUDINAL STABILITY OF  
FLARE-STABILIZED BODIES AT HYPERSONIC P.E.  
Fitzgerald, Jr. (NASA) Mar. 1962 ~~50~~ p

N72-72996

Unclas  
00/99 30867

NATIONAL AERONAUTICS AND SPACE ADMINISTRATION  
WASHINGTON

March 1962

50

NATIONAL AERONAUTICS AND SPACE ADMINISTRATION

TECHNICAL MEMORANDUM X-664

THE EFFECT OF BOW-SHOCK—FLARE-SHOCK INTERACTION ON  
THE STATIC LONGITUDINAL STABILITY OF FLARE-STABILIZED BODIES

AT HYPERSONIC SPEEDS\*

By Paul E. Fitzgerald, Jr.

GROUP 4

Downgraded at 3 year  
intervals; declassified  
after 12 years

SUMMARY

Force and moment data from previously published papers have been presented to show that flare-stabilized bodies at hypersonic speeds experience a decrease or complete loss in static longitudinal stability at certain definite angles of attack. The reason for this decrease in stability and the mechanism by which it occurs is explained. Pressure data and schlieren photographs obtained from tests at a Mach number of 8.5 of two flare-stabilized missile bodies having a fineness ratio of 10 are presented to substantiate this explanation. Tests of these two missiles were conducted over an angle-of-attack range of  $0^\circ$  to  $27^\circ$  at a Reynolds number of approximately  $9.3 \times 10^6$  based on model length.

A decrease in stability of flare-stabilized bodies at hypersonic speeds is shown to be caused by a bow-shock—flare-shock interaction phenomenon. Pressure tests indicate that the nose bluntness of high-fineness-ratio bodies has no influence on the angle of attack at which this phenomenon occurs. From comparisons of force and moment data at Mach numbers of 6.0 and 8.5, it appears that the angle of attack at which this loss in stability occurs decreases as Mach number increases. Analytical approximations of the pressures on the  $0^\circ$  meridian of the two models tested at a Mach number of 8.5 are in reasonably good qualitative agreement with the data.

INTRODUCTION

It has been noticed from, although not noted in, several papers dealing with flare-stabilized bodies at hypersonic speeds (refs. 1, 2,

\*Title, Unclassified.

and 3) that there is a considerable decrease or complete loss of longitudinal stability at the higher angles of attack. (The term stability as used herein refers to trends in the curve for pitching-moment coefficient plotted against angle of attack at any given angle of attack, that is, if the slope of this pitching-moment curve becomes less negative, this trend is termed a decrease in stability even though the value of pitching-moment coefficient is still increasing negatively with increasing angle of attack.) It was noticed that this decrease in stability takes place only when the angle of attack is such as to cause the intersection of the bow shock and the flare shock to occur in the vicinity of the flare. It is the purpose of this paper to explain why this decrease in stability occurs and the mechanism by which it occurs. To verify this explanation, pressure data were obtained on two flare-stabilized missile bodies having a fineness ratio of 10. One of these missile bodies had an ogive nose with a fineness ratio of 5, and the other had a hemispherical nose with a fineness ratio of  $\frac{1}{2}$ . Longitudinal

force and moment data were also obtained on the ogive-nosed body. These tests were conducted in the Langley 22-inch Mach 8.5 tunnel at a Reynolds number of about  $9.3 \times 10^6$  based on model length and over an angle-of-attack range from  $0^\circ$  to  $27^\circ$  for the pressure tests and  $-5^\circ$  to  $30^\circ$  for the force and moment tests. To introduce the problem at hand, several plots for the variation of pitching-moment coefficient, normal-force coefficient, and axial-force coefficient with angle of attack have been reproduced from references 1, 2, and 3. One figure showing previously unpublished control effectiveness data at a Mach number of 6.01 is also included.

Three methods of predicting the pressure distribution on the  $0^\circ$  meridian of the cylinder and cone frustum have been employed and the predictions are compared with data of the present pressure tests.

## SYMBOLS

Force and moment coefficients are referred to the body axis system as shown in figure 1, and pitching-moment coefficients at Mach numbers of 6.01 and 8.5 are referenced to locations at 50 percent, 55.5 percent, and 58.35 percent of the body length.

A cross-sectional area of cylindrical portion of body, sq in.

$C_A$  axial-force coefficient,  $\frac{F_A}{q_\infty A}$

$\Delta C_A$  change in axial-force coefficient due to flare deflection

$C_N$	normal-force coefficient, $\frac{F_N}{q_\infty A}$
$\Delta C_N$	change in normal-force coefficient due to flare deflection
$C_m$	pitching-moment coefficient, $\frac{M_Y}{q_\infty A d}$
$\Delta C_m$	change in pitching-moment coefficient due to flare deflection
$C_m'$	pitching-moment coefficient from reference 1
$C_m''$	pitching-moment coefficient from reference 2
$C_{p,max}$	maximum pressure coefficient
$F_A$	axial force, lb
$F_N$	normal force, lb
$M$	Mach number
$M_Y$	pitching moment, in-lb
$d$	diameter of cylindrical portion of body, in.
$p_\infty$	free-stream static pressure, lb/sq in. abs
$p_l$	local static pressure, lb/sq in. abs
$q_\infty$	free-stream dynamic pressure, lb/sq in. abs
$x$	distance along body longitudinal axis (X-axis) measured from nose, in.
$\alpha$	angle of attack, deg
$\alpha'$	angle of attack from reference 1, deg
$\alpha''$	angle of attack from reference 2, deg
$\phi$	roll angle of body meridian on which pressure orifices are located (see fig. 1), deg

L  
1  
8  
1  
3

## APPARATUS AND TEST CONDITIONS

### Tunnel

Tests were conducted in the Langley 22-inch Mach 8.5 tunnel, which is a blowdown-to-atmosphere type of tunnel, a schematic drawing of which is shown in figure 2. The tunnel has a three-dimensional nozzle, a cylindrical 22-inch-diameter test section, and is equipped with an annular air ejector and a fixed 19.64-inch-diameter second minimum. An annular water injection system downstream of the test section is employed to cool the air and avoid overheating the exit piping.

The tunnel is capable of operating at a maximum pressure of 2,700 lb/sq in. gage at a temperature of 1,050° F and 1,800 lb/sq in. gage at temperatures from 1,050° F to 1,400° F. Flow to the tunnel emanates from a 20,000-cubic-foot tank field, passes through a Dowtherm heat exchanger which raises the temperature to 600° F, and then passes through a 6,800-kilowatt electric heater which raises the temperature to running level before reaching the tunnel settling chamber.

Models are supported in the tunnel by a vertical circular-arc strut (fig. 3) which allows an angle-of-attack range of -10° to 30°. The angle of attack is measured by using an optical system which is described in reference 4.

The schlieren apparatus used with this tunnel is a single-pass horizontal Z light path with a horizontal knife edge. The light source used for continuous viewing and for taking schlieren photographs is a mercury vapor arc lamp having a flash duration of from 2 to 6 microseconds. Several 8-foot mercury manometer boards to measure local pressures on the model and a gage board to measure tunnel stagnation and ejector pressures are photographed during test runs to record pressure data. Normal-force and pitching-moment data were obtained on one model of the present tests by using a six-component water-cooled internal strain-gage balance.

Tunnel calibration shows that the local Mach number in the model test region may vary  $\pm 0.11$  from the Mach number of 8.5; whereas the average deviation from a Mach number of 8.5 for the present tests (considering model location in the tunnel) is -0.04.

### Test Conditions

For the present tests, the stagnation pressure, the temperature, and the ejector pressure were maintained at approximately 1,800 lb/sq in. gage, 1,040° F, and 1,400 lb/sq in. gage, respectively. Force data were

obtained over an angle-of-attack range of  $-5^\circ$  to  $30^\circ$  and pressure data, over an angle-of-attack range of  $0^\circ$  to  $27^\circ$ . Test Reynolds number was constant at about  $9.3 \times 10^6$  based upon body length.

### Models

Two flare-stabilized missile models having a fineness ratio of 10 (shown in fig. 4) have been tested; one having an ogive nose with a fineness ratio of 5 (configuration I), and the other having a hemispherical nose with diameter the same as the cylindrical body (configuration II). Both have cylindrical bodies and identical  $10^\circ$  half-angle flared skirts. Fourteen 0.040-inch-diameter static pressure orifices were located along a meridian plane on the rearward portion of the cylinder and along the entire length of the flare. Pressure orifice locations are identical for each model. Since the models are symmetrical about their longitudinal axes, each model was rolled from  $\phi = 0^\circ$  to  $90^\circ$  in steps of approximately  $30^\circ$ , and the data obtained correspond to a pressure distribution over the lower half of the cylinder and flare.

### ACCURACY

Maximum probable error in force and moment coefficients for previously unpublished data are presented, together with maximum variation in local free-stream Mach number and local static pressure ratio, as follows:

$C_N$ . . . . .	$\pm 0.11$
$C_A$ . . . . .	$\pm 0.02$
$C_m$ . . . . .	$\pm 0.24$
$\Delta C_N$ . . . . .	$\pm 0.17$
$\Delta C_A$ . . . . .	$\pm 0.03$
$\Delta C_m$ . . . . .	$\pm 0.25$
$M$ . . . . .	$\pm 0.11$
$p_l/p_\infty$ , percent of measured value . . . . .	$\pm 8$
$\alpha$ (error in angle-measuring mechanism only), deg . . . . .	$\pm 0.10$
$\phi$ , deg . . . . .	$\pm 0.30$

One exception to the accuracy given for pressure ratio is the pressure ratio at station 16.2, which may be in error by 1 pressure ratio at very low angles of attack and, hence, the error would be greater than 8 percent of the measured value. This larger error was due to a "slow" pressure tube.

## ANALYSIS, RESULTS, AND DISCUSSION

Figures 5 to 9 are presented to illuminate a stability problem which has been noticed to occur in flare-stabilized bodies at hypersonic speeds. Figure 5 (taken from ref. 1) shows that the longitudinal stability of two missile bodies (fineness ratio of about 4) at a Mach number of 8 decreases with increasing angle of attack above an angle of attack of  $17^\circ$ . This decrease in stability occurs even though the center of gravity is reasonably far forward (approximately 30 percent of body length).

Figure 6 from reference 2 shows that the longitudinal stability of the low-fineness-ratio Mercury spacecraft in the escape configuration at a Mach number of 9.6 decreases abruptly at an angle of attack of about  $8^\circ$ , and the spacecraft in the exit configuration becomes completely unstable at this angle of attack. Although the possible error in measurement as shown in figure 6 is large, the trend toward instability at an angle of attack of about  $8^\circ$  is still apparent. Figures 7 and 8 (at Mach numbers of 6.0 and 8.5, respectively) show data obtained on a missile body with a fineness ratio of 10 (configuration I) plotted with center-of-gravity locations at 50.00, 55.50, and 58.35 percent of the body length. These three center-of-gravity locations were chosen to show three specific types of influence that could occur: first, with the center of gravity far enough forward (50.00 percent location) the decrease in stability is negligible; second, with the center-of-gravity location at 55.50 percent the missile goes from a stable condition to a condition of neutral stability; and third, with the center-of-gravity location at 58.35 percent the missile goes from a neutrally stable condition to an unstable condition. Figures 7 and 8 show that this decrease in longitudinal stability occurs at an angle of attack of approximately  $20^\circ$  at a Mach number of 6.0 and approximately  $15^\circ$  at a Mach number of 8.5. These data indicate that the angle of attack at which this decrease in stability occurs decreases as Mach number increases. Figure 9 shows data at a Mach number of 6.0 in which the  $10^\circ$  flare of configuration I is deflected to provide longitudinal control for the missile. In this case, there is a decrease in control effectiveness (as evidenced by the decreasing amount of  $-\Delta C_m$ ) above an angle of attack of about  $15^\circ$ .

Where schlieren photographs or shadowgraphs were available (refs. 1 and 2), it may be seen that the decrease in longitudinal stability takes place only when the intersection of the bow shock and the flare shock occurs in the region adjacent to the flare. The loss in stability of these flare-stabilized bodies is directly associated with the proximity of this shock intersection to the flared surface and is explained in the following discussion.

L  
1  
8  
1  
3

When two shocks of the same family intersect, the pressure rise across the two shocks may be greater than that across the coalesced shock, because of the more nearly isentropic nature of the two converging compressions (refs. 5 and 6). Reference is made in this regard to figure 10 which shows a cross section (through a  $\phi = 0^\circ$  body meridian) of the flow field in the vicinity of the flare on a flare-stabilized body at some angle of attack. From what has just been mentioned, the flow as it passes from region I, through region II, and into region III can experience a greater increase in pressure than the flow passing from region I into region VI. If second-order waves are neglected in these regions and the assumption is made that the flow is two dimensional, then an expansion emanating from the bow-shock—flare-shock intersection must take place which separates the regions of differing pressure. This expansion must necessarily make the flow angle in regions IV and VI greater than that in region III, and the coalesced shock adjusts its angle accordingly. Ferri, discussing supersonic shock interactions in reference 5, states that this expansion in many cases is negligible. It will be shown, however, that this is not necessarily the case at hypersonic speeds and that this expansion can have a considerable influence on a surface adjacent to it. Again, from figure 10, it is seen that the expansion is reflected off the flare back toward, and is absorbed into, the coalesced shock. Hence, the flow passing from region IV to region V again experiences a decrease in pressure approximately equal to the decrease between regions III and IV. Therefore, the pressure on the surface of the flare in region V can be considerably less than that on the surface in region III, the amount being dependent on the strength of the expansion. The three-dimensional surface area of the flare that is influenced by this low-pressure region would increase as the angle of attack increases and the bow-shock—flare-shock intersection moves progressively forward on the flare. This forward movement of the shock intersection as angle of attack increases is obvious because the bow shock moves closer to the body and the flare shock becomes steeper (because of the lower Mach number behind the bow shock). It is the low-pressure region on the flare that causes the decrease in longitudinal stability on the various bodies that were previously mentioned. It should also be mentioned that although for the two-dimensional case the pressure and flow direction is the same in regions IV and VI, and V and VII, the velocities in these four regions would not be the same. These velocity differences give rise to a slipstream or vortex sheet which again emanates from the bow-shock—flare-shock intersection and passes between these four regions as shown on figure 10.

Pressure tests of two flare-stabilized missile bodies with a fineness ratio of 10 at a Mach number of 8.5 substantiate the results of the previous discussion. Figure 11 presents pressure-distribution data for configuration I at angles of attack from  $0^\circ$  to  $27^\circ$  along with corresponding schlieren photographs for each angle of attack. It can be seen from the pressure data and schlieren photograph of the body at an



angle of attack of  $0^\circ$  (figs. 11(a) and (b)) that the laminar boundary layer is separated far forward on the body and emerges the major portion of the flare, pressures on the flare being only 1 pressure ratio higher than on the cylinder. Schlieren photographs indicate that at an angle of attack of  $6^\circ$ , the separated region on the lower surface of the missile has been, for the most part, washed away by the three-dimensional relieving effects of the cylindrical body; in addition, the flow on the upper surface of the cylinder and flare appears to be completely separated. At test angles of attack of  $6^\circ$  or greater for configuration I, (fig. 11), the pressure along the  $0^\circ$  and  $30^\circ$  meridians peaks at station 15 (just downstream of the cylinder-flare junction) and then drops off. (Nominal meridian values of  $0^\circ$ ,  $30^\circ$ ,  $60^\circ$ , and  $90^\circ$  are used in the discussion rather than the absolute values of  $\phi$  which are shown in figs. 11 and 12.) This pressure peak is believed to be caused by the fact that the flow passing through the flare shock close to the cylinder-flare junction experiences something close to a two-dimensional pressure rise, resulting in the peak pressure, and then decreases to a pressure closer to the theoretical cone value as the flow continues along the flare. However, the pressure along the  $0^\circ$  and  $30^\circ$  meridians again increases to a second peak value, approximately equal in value to that of the first peak. This second rise in pressure is due to the entropy gradient which exists in the shock layer between the bow shock and the model. This gradient causes a slightly rearward curvature in the flare shock which gives rise to a series of minute compression waves in the region between the flare shock and the flare. These compression waves, which may be reflected back and forth between the surface of the flare and the flare shock, raise the pressure on the flare.

From the schlieren photograph in figure 11(c) it can be seen that at an angle of attack of  $15^\circ$ , the bow-shock-flare-shock intersection is located in the vicinity of the trailing edge of the flare, and the pressure on the  $0^\circ$  meridian (fig. 11(d)) has started to decrease slightly at station 17.7. At an angle of attack of  $18^\circ$ , with the shock intersection farther forward, the pressure from stations 17 to 18 on the  $0^\circ$  meridian has decreased by a pressure ratio value of approximately 12, and in this case, the low-pressure region is extended around the flare to the  $30^\circ$  meridian. (See figs. 11(e) and 11(f).) This decrease in pressure is a direct result of the expansion fan which emanates from the shock intersection. Figures 11(g) to 11(l) show that as the angle of attack increases from  $21^\circ$  to  $27^\circ$ , the area of the influence of this expansion fan increases to include approximately half the length of the flare and around the flare at least to the  $60^\circ$  meridian. At an angle of attack of  $27^\circ$ , on the  $0^\circ$  meridian, the maximum loss in pressure due to this shock interference effect amounts to 16 pressure ratios or approximately half the pressure increase on the flare due to the presence of the flare on the body.

In order to determine the influence of nose shape on this shock interaction phenomenon, configuration II with a hemispherical nose was tested and the results are presented in figure 12. There are several major differences between the pressure data of configurations I and II. The greater extent of high-entropy air behind the bow shock of the blunt-nosed body is clearly evidenced by the lower pressures on the flare (fig. 12(b)) up to an angle of attack of about  $9^\circ$  and the increased distance between flare and shock. The fact that strong bow shocks associated with blunter bodies give rise to greatly decreased dynamic pressures in the region of a flare has been noted in several papers dealing with flare-stabilized bodies at hypersonic speeds (for example, ref. 7). Above an angle of attack of  $12^\circ$ , the pressures on the body and flare of configuration II are higher than those of configuration I. (Compare figs. 11 and 12.) The difference in pressure at any one point on the flare increases as angle of attack increases so that at  $24^\circ$ , the maximum pressure on the flare of configuration II is 8 pressure ratios higher than that on flare of configuration I. The reason for this higher flare pressure on the blunt-nosed configuration is not evident. The significant fact that should be noticed, however, is that for both configurations the angle of attack at which the bow-shock—flare-shock interaction begins to be felt is the same, that is,  $15^\circ$ . Also, for any constant angle of attack above  $15^\circ$ , the flare area which is influenced by this phenomenon is the same and the magnitude of the pressure loss (in percent of pressure rise on the flare due to the presence of the flare) is about the same for both configurations.

#### THEORETICAL APPROXIMATIONS

In order to show that this bow-shock—flare-shock interaction phenomenon can be approximated empirically or theoretically, figures 13 and 14 are presented for configurations I and II, respectively. Comparison is made with data taken on the  $0^\circ$  meridian of these configurations at the highest test angle of attack for each model.

If it is assumed that the cylinder-frustum portion of each model is a two-dimensional flat plate with a  $10^\circ$  wedge, then two-dimensional shock-expansion theory (calculations from ref. 8), using shock angles and stand-off distances which were measured from schlieren photographs, gives a reasonably good approximation of the gross effects of the shock interaction (figs. 13 and 14).

Since schlieren photographs in many cases may not be available, it was then assumed that for high-fineness-ratio bodies at high Mach numbers and high angles of attack ( $\alpha > 18^\circ$ ), the bow shock would be parallel to

the cylindrical portion of the body and, hence, the stand-off distance of the bow shock could be determined from reference 9 by using cross-flow Mach number. With the use of two-dimensional pressure values for the cylindrical portion of the body and cone shock angle and pressure values for the frustum, the pressure distribution was again calculated. Figures 13 and 14 show that although the magnitude of the pressure decrease on the  $0^\circ$  meridian of the flare can again be reasonably well approximated, the pressure at any given point along this meridian can be in error by a considerable amount.

As would be expected, a Newtonian calculation using  $C_{p,\max}$  of 1.83 does not show the effect of the shock interaction nor does it give an accurate account of the magnitude of the pressure on the flare.

L  
1  
8  
1.  
3

### CONCLUSIONS

An analysis of data obtained from two flare-stabilized missile bodies having a fineness ratio of 10 leads to the following conclusions:

1. Decrease in stability of flare-stabilized bodies at high angles of attack and at hypersonic speeds may be due to a bow-shock—flare-shock interaction phenomenon, which leads to a pressure decrease on the flare.
2. The angle of attack at which this interaction phenomenon occurs for high-fineness-ratio bodies at a Mach number of 8.5 is independent of nose bluntness.
3. The magnitude of the pressure decrease on the  $0^\circ$  meridian of a flare due to this shock interference effect can be analytically approximated.

Langley Research Center,  
National Aeronautics and Space Administration,  
Langley Air Force Base, Va., December 19, 1961.

## REFERENCES

1. Myers, J. R., and Burchfield, C. G.: Static Stability, Pressure Distribution Boundary-Layer Investigation, and Heat Transfer Tests of Lockheed Polaris Re-Entry Body at Mach Number 8. AEDC-TN-60-183 (Contract No. AF 40(600)-800 S/A 11(60-110)), Arnold Eng. Dev. Center, Oct. 1960.
2. Everhart, Philip E., and Bernot, Peter T.: Measurements of the Surface Flows, Heat Transfer, Pressure Distribution, and Longitudinal Stability of a Mercury Capsule Model at Mach Numbers of 6.9 and 9.6. NASA TM X-458, 1961.
3. Ashby, George C., Jr.: Longitudinal Aerodynamic Characteristics of Five Hypersonic Missile Configurations at Mach Numbers From 2.01 to 6.01. NASA TM X-526, 1961.
4. Ashby, George C., Jr., and Fitzgerald, Paul E., Jr.: Longitudinal Stability and Control Characteristics of Missile Configurations Having Highly Swept Cruciform Fins and a Number of Trailing-Edge and Fin-Tip Controls at Mach Numbers From 2.21 to 6.01. NASA TM X-335, 1961.
5. Ferri, Antonio: Elements of Aerodynamics of Supersonic Flows. The Macmillan Co., 1949, pp. 73-76.
6. Shapiro, Ascher H.: The Dynamics and Thermodynamics of Compressible Fluid Flow. Vol. I. The Ronald Press Co., 1953, pp. 558-559.
7. Penland, Jim A.: Static Longitudinal Stability of a Missile Configuration With Various Nose Shapes and Flared Afterbodies at a Mach Number of 6.82. NASA TM X-274, 1960.
8. Ames Research Staff: Equations, Tables, and Charts for Compressible Flow. NACA Rep. 1135, 1953. (Supersedes NACA TN 1428.)
9. Kaattari, George E.: Predicted Shock Envelopes About Two Types of Vehicles at Large Angles of Attack. NASA TN D-860, 1961.

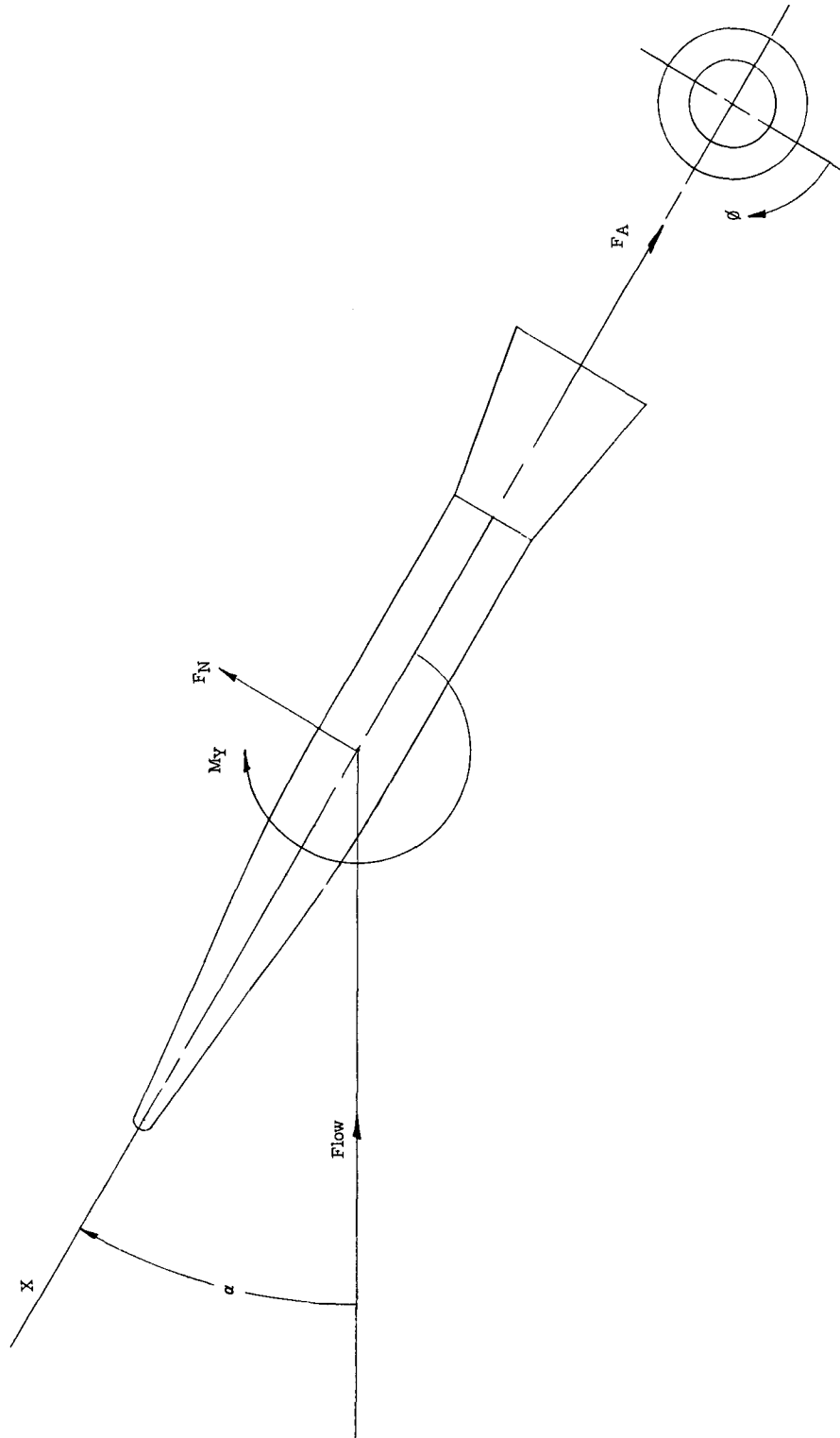


Figure 1.- Forces, moments, and angle designation for force tests. Arrows indicate positive directions of forces, moments, and angles.

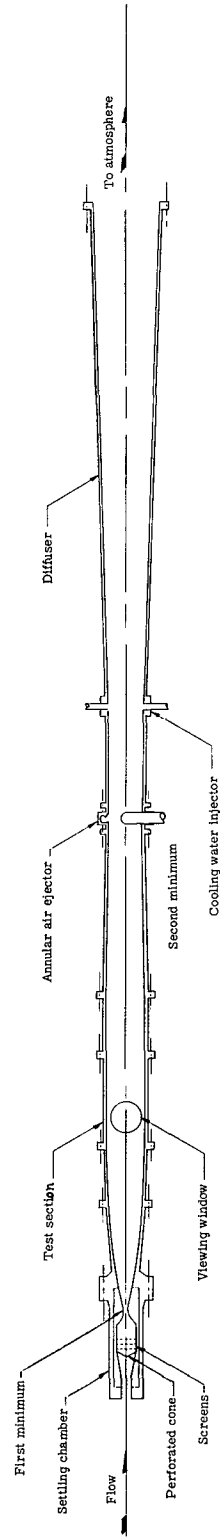


Figure 2.- Schematic diagram of Langley 22-inch Mach 8.5 tunnel.

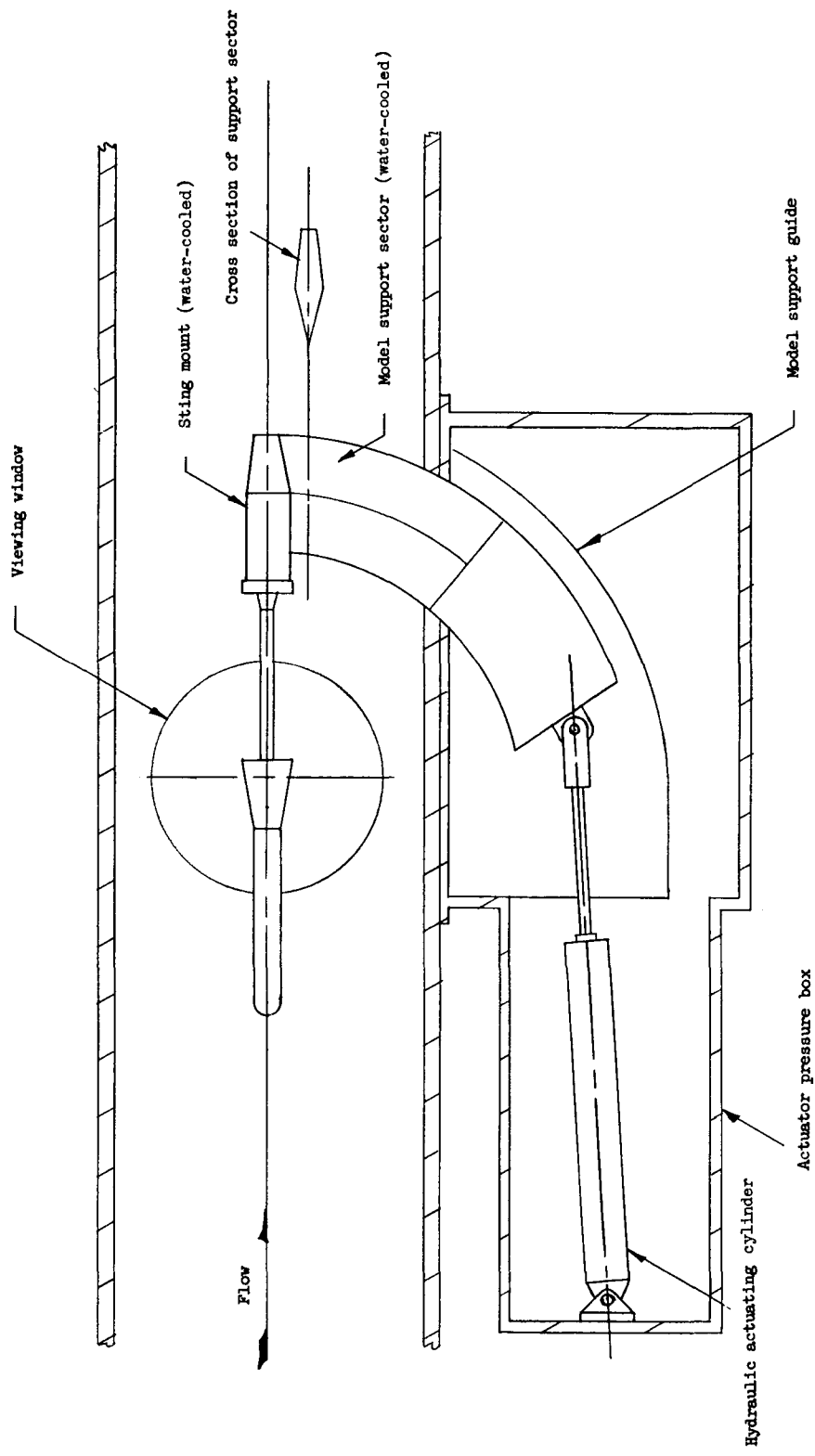


Figure 3.- Schematic diagram of model support system.

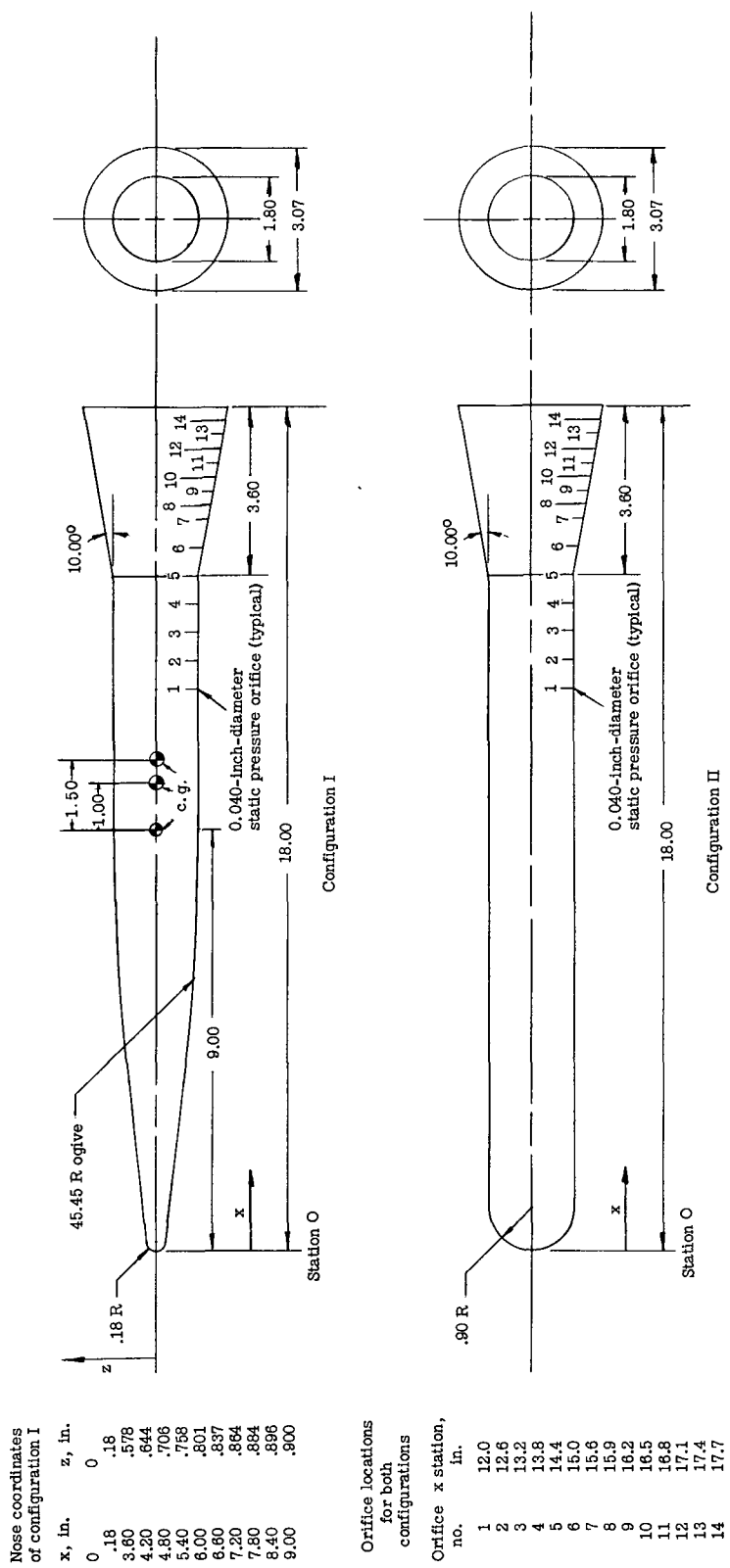


Figure 4.- Details and basic dimensions of configurations I and II.  
All dimensions are in inches.



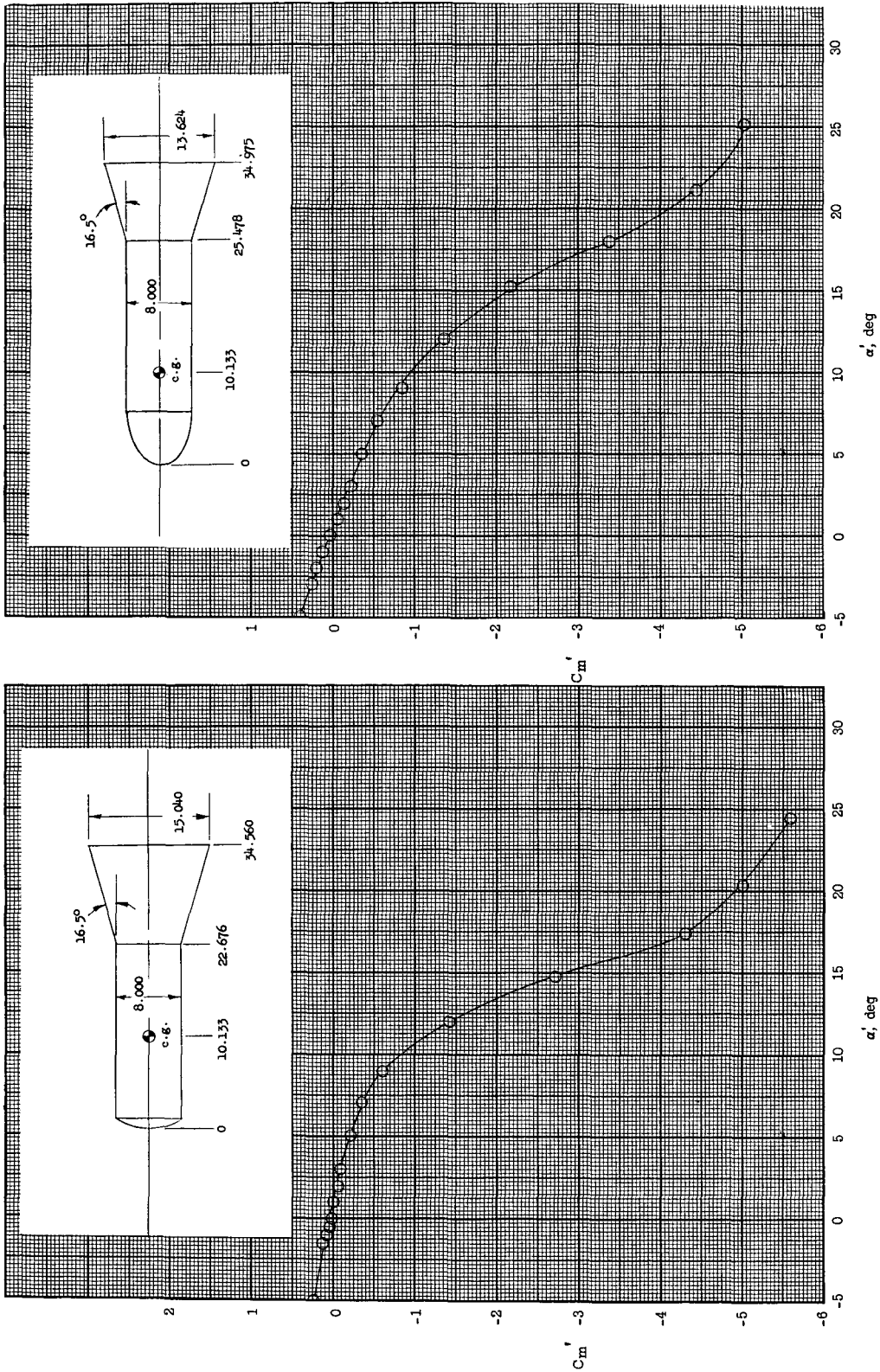
(a) Configuration N<sub>6</sub>B<sub>15</sub>S<sub>30</sub>.(b) Configuration N<sub>24</sub>B<sub>18</sub>S<sub>16A</sub>.

Figure 5.- Pitching-moment coefficient plotted against angle of attack for two configurations having a fineness ratio of 4.3 from reference 1.  $M = 8$ .

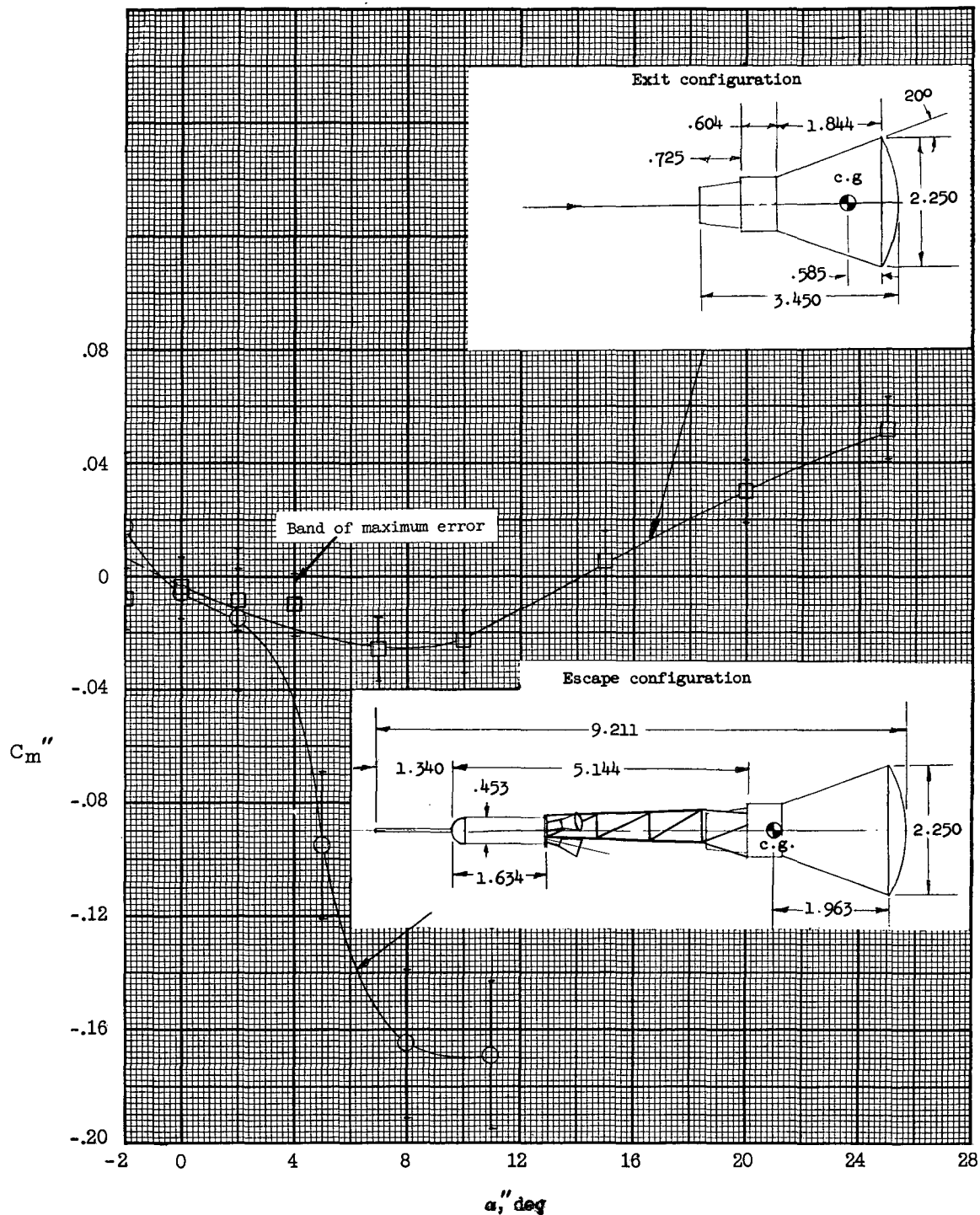


Figure 6.- Pitching moment for exit and escape configurations of Mercury spacecraft at  $M = 9.6$  from reference 2.

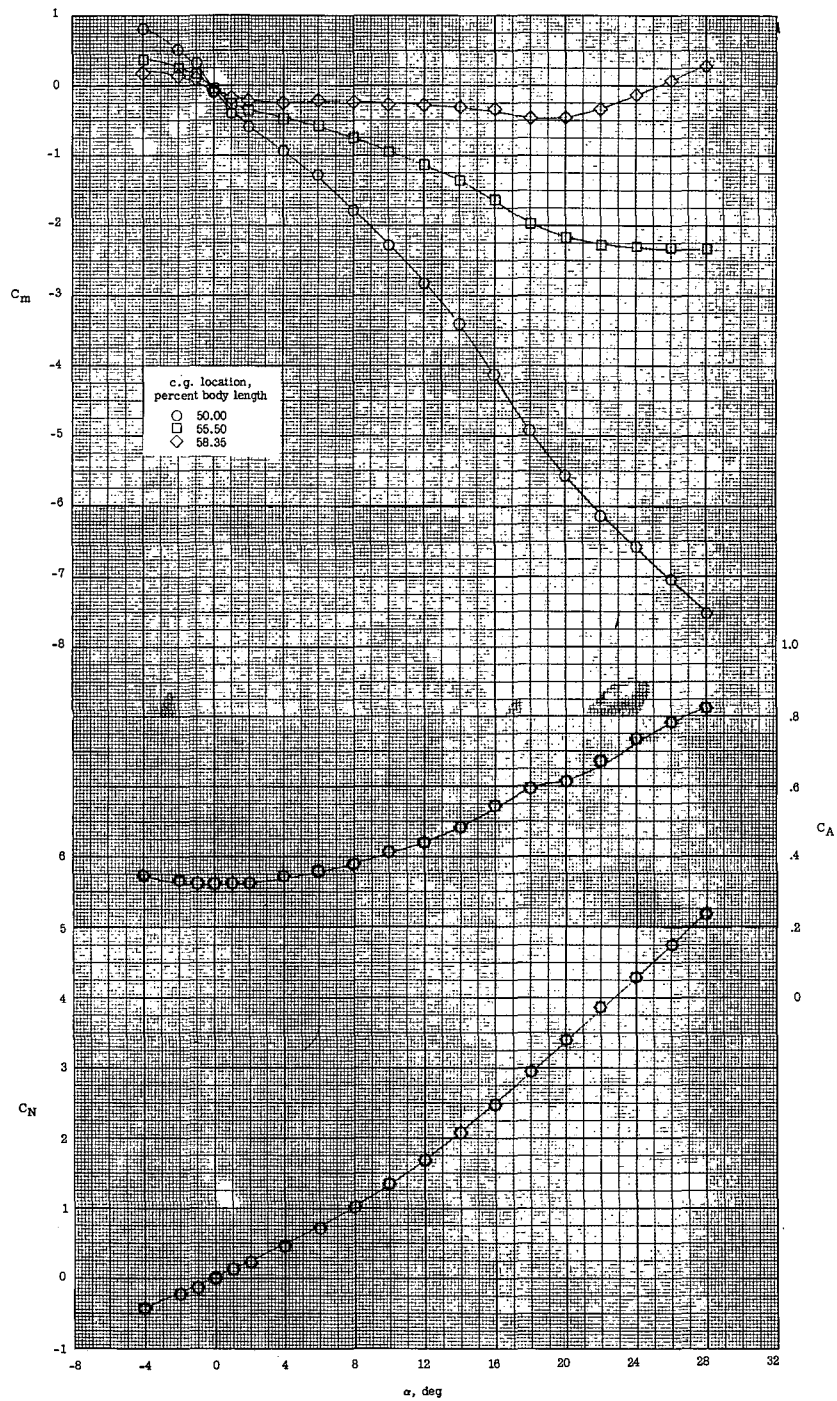


Figure 7.- Longitudinal characteristics of configuration I at a Mach number of 6.0 for three center-of-gravity locations. Data from reference 3.

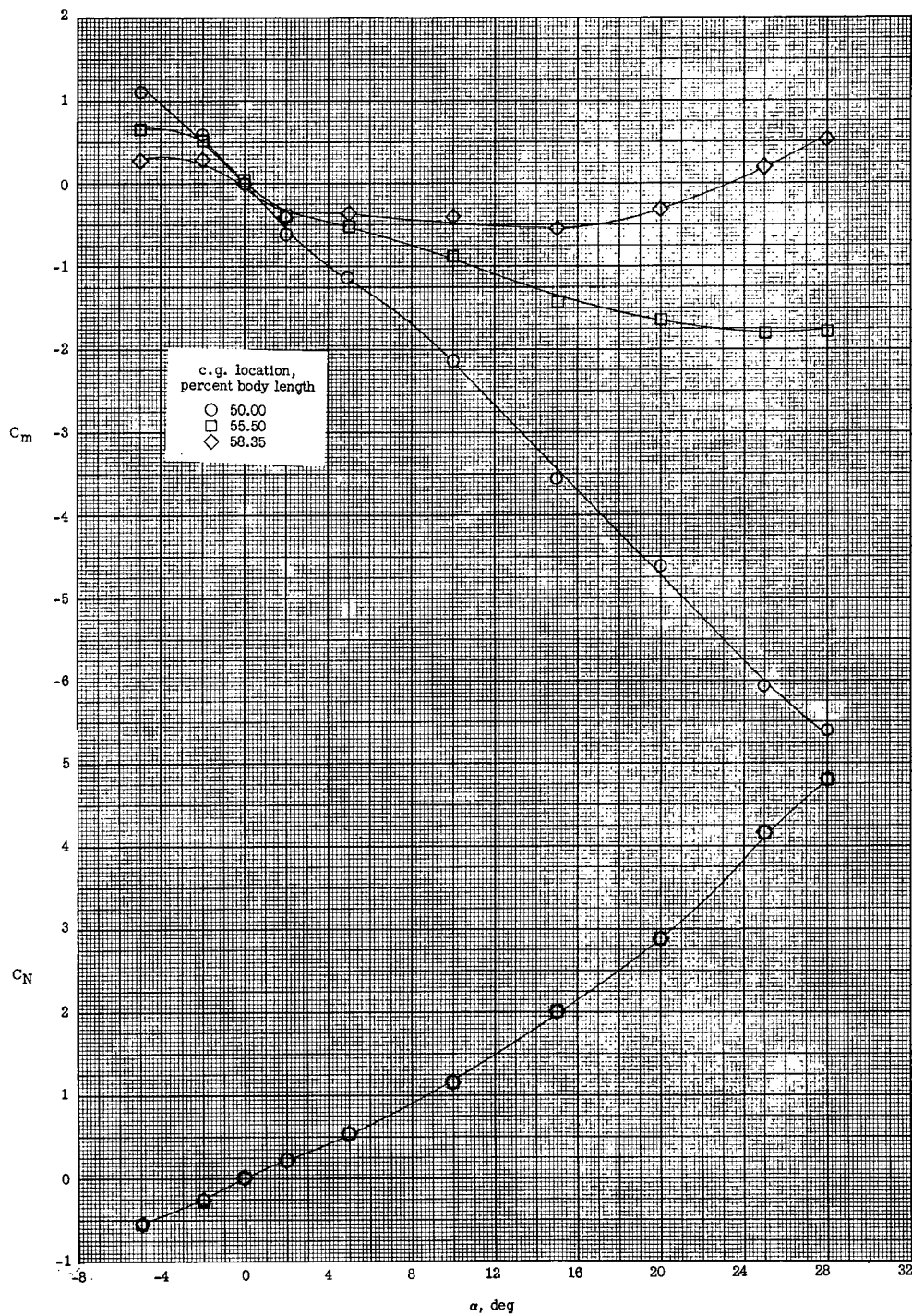


Figure 8.- Longitudinal characteristics of configuration I at  $M = 8.5$ , for three center-of-gravity locations.

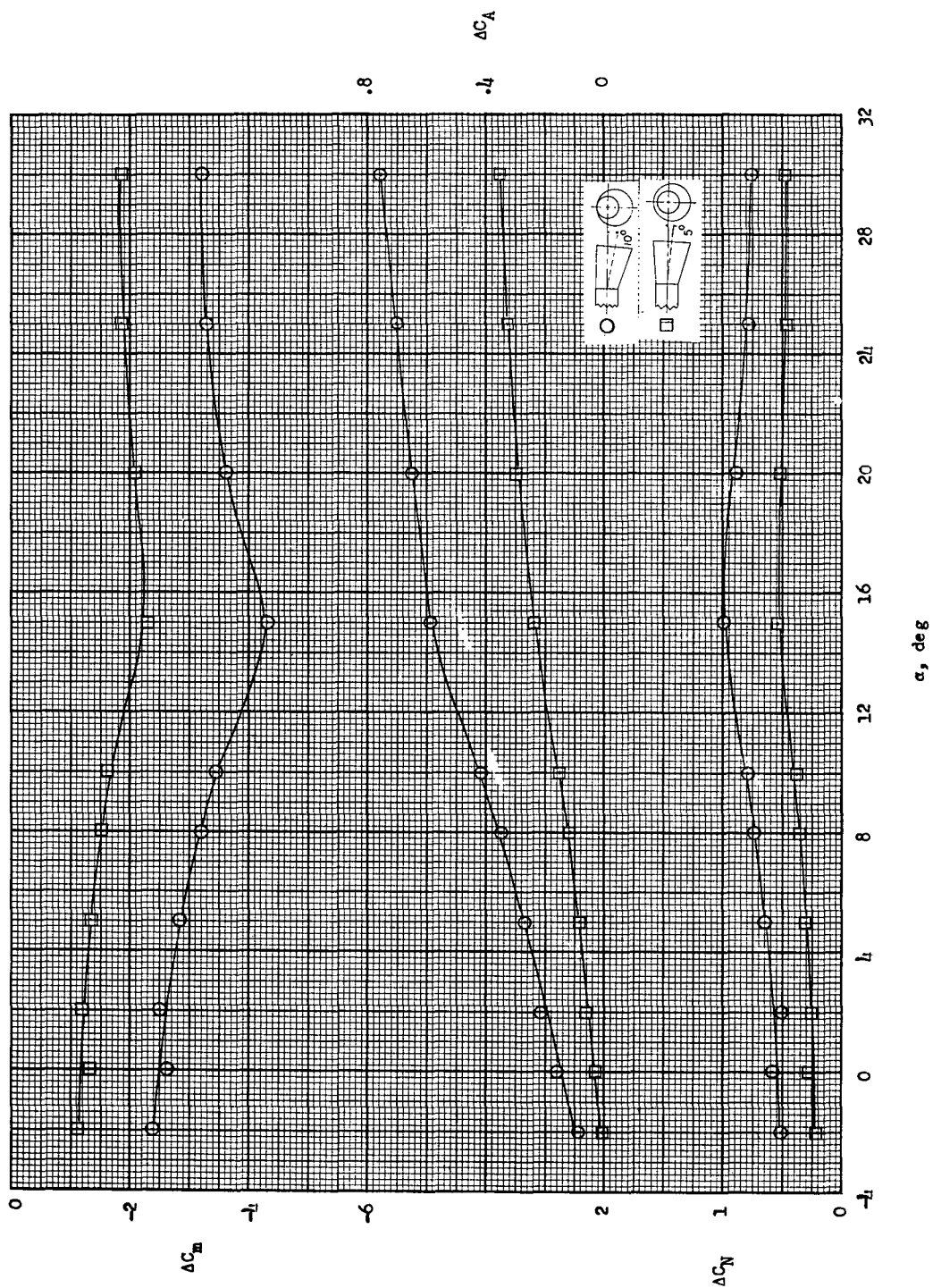


Figure 9.- Control effectiveness parameters plotted against  $\alpha$  for configuration I with flares deflected  $5^\circ$  and  $10^\circ$ .  $M = 6.0$ .

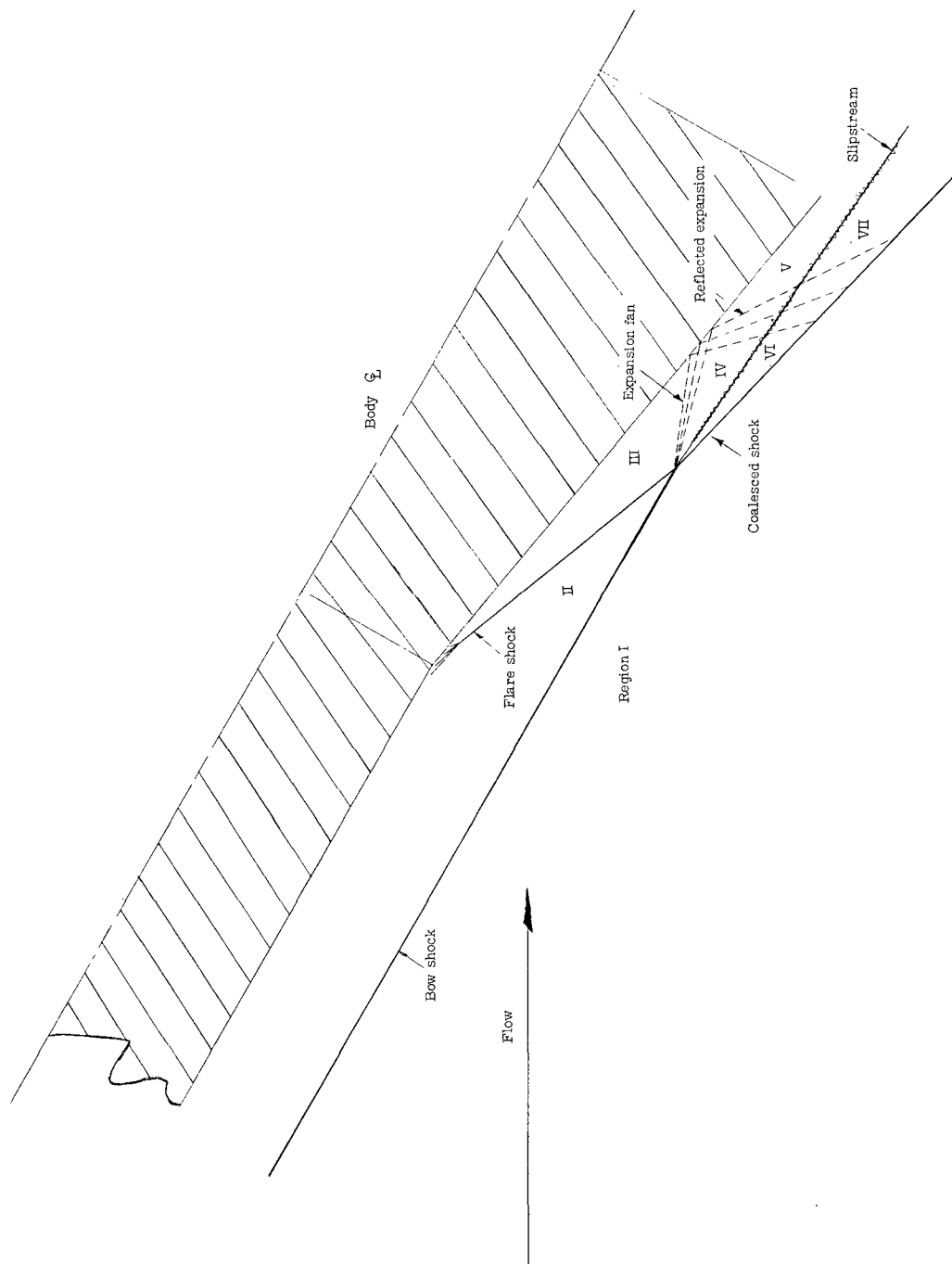
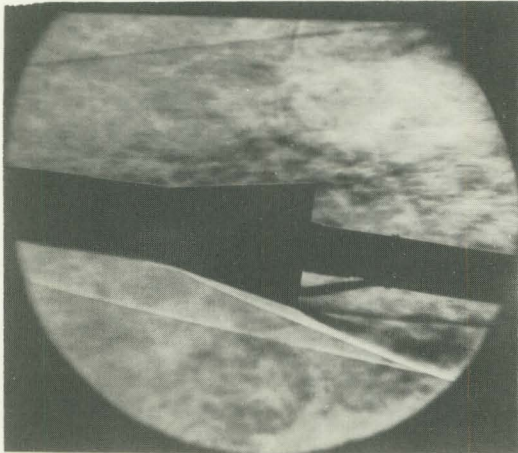
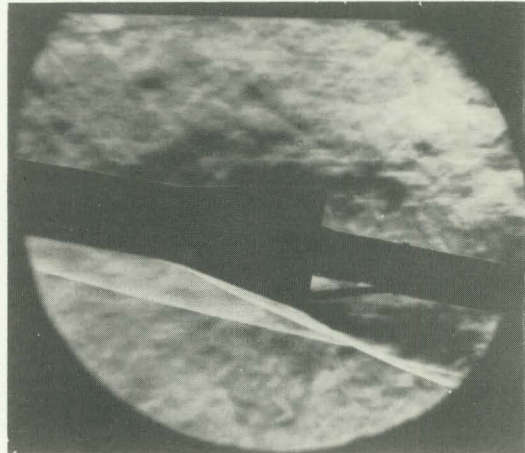
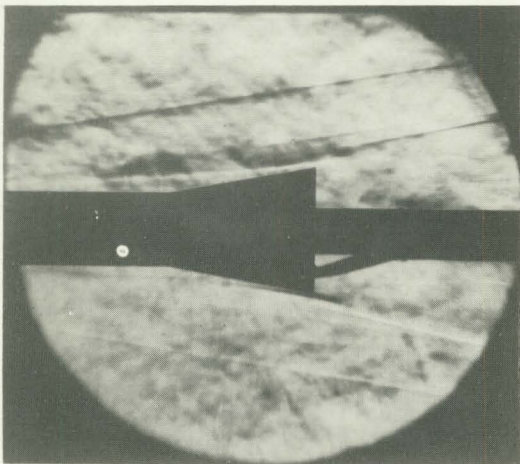
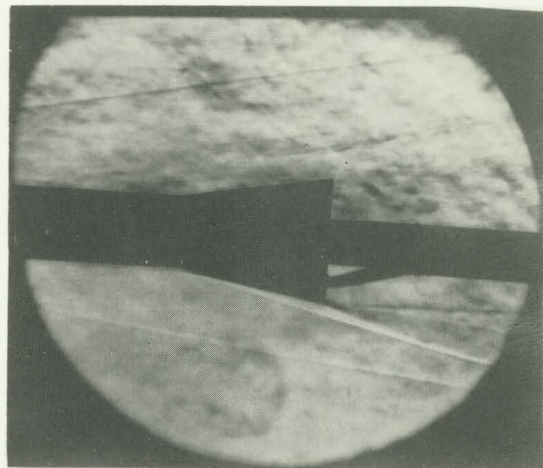


Figure 10.- Cross section of aft portion of flare-stabilized body showing shock interaction pattern.

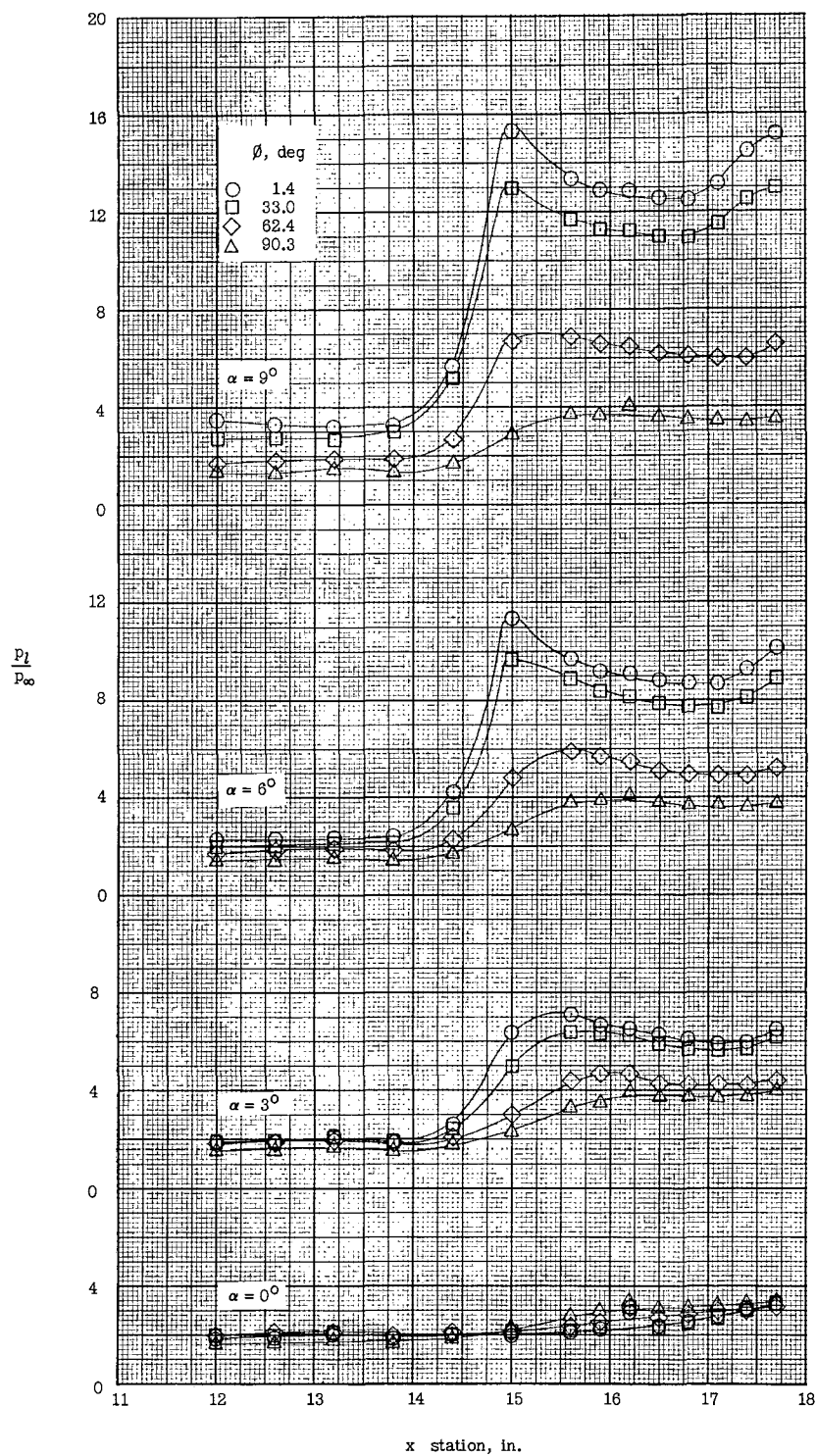


~~CONFIDENTIAL~~ $\alpha = 6^\circ$  $\alpha = 9^\circ$  $\alpha = 0^\circ$  $\alpha = 3^\circ$ 

(a) Schlieren photographs;  $\alpha = 0^\circ, 3^\circ, 6^\circ$ , and  $9^\circ$ . L-62-3

Figure 11.- Schlieren photographs and pressure data on aft portion of configuration I over an angle-of-attack range from  $0^\circ$  to  $27^\circ$ .  
 $M = 8.5$ .

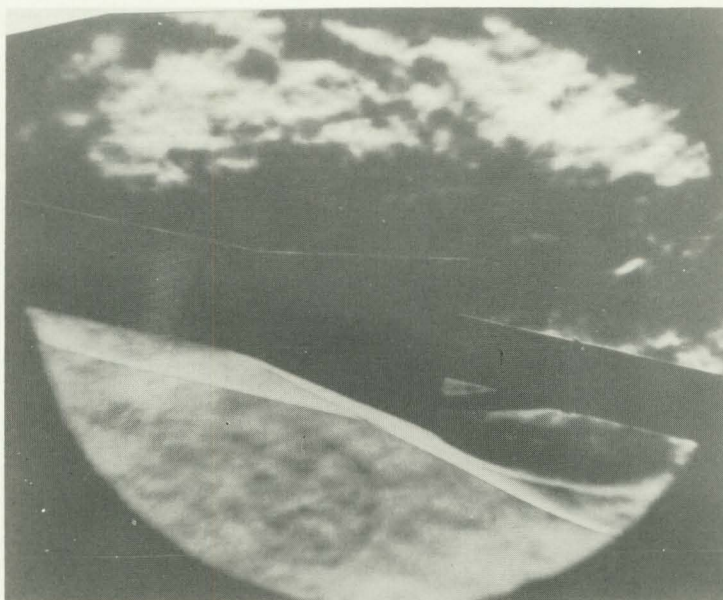
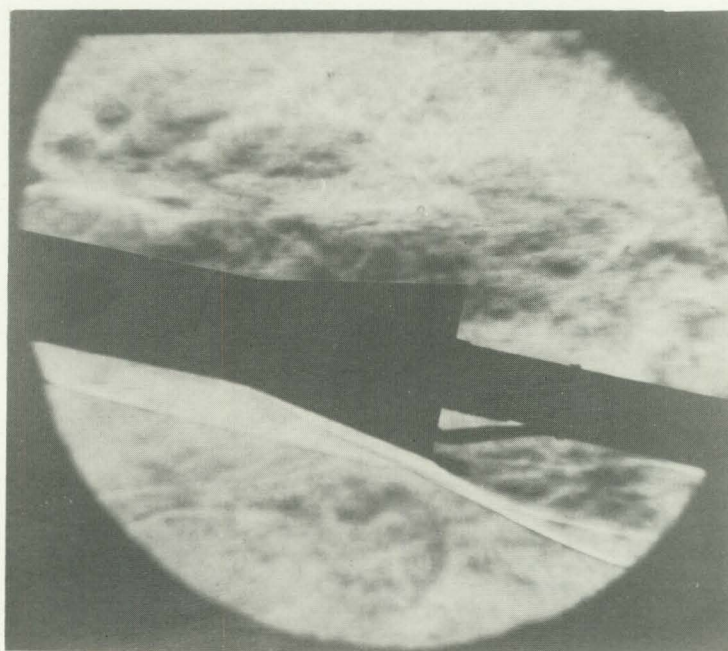
~~CONFIDENTIAL~~



(b) Pressure data;  $\alpha = 0^\circ, 3^\circ, 6^\circ$ , and  $9^\circ$ .

Figure 11.- Continued.

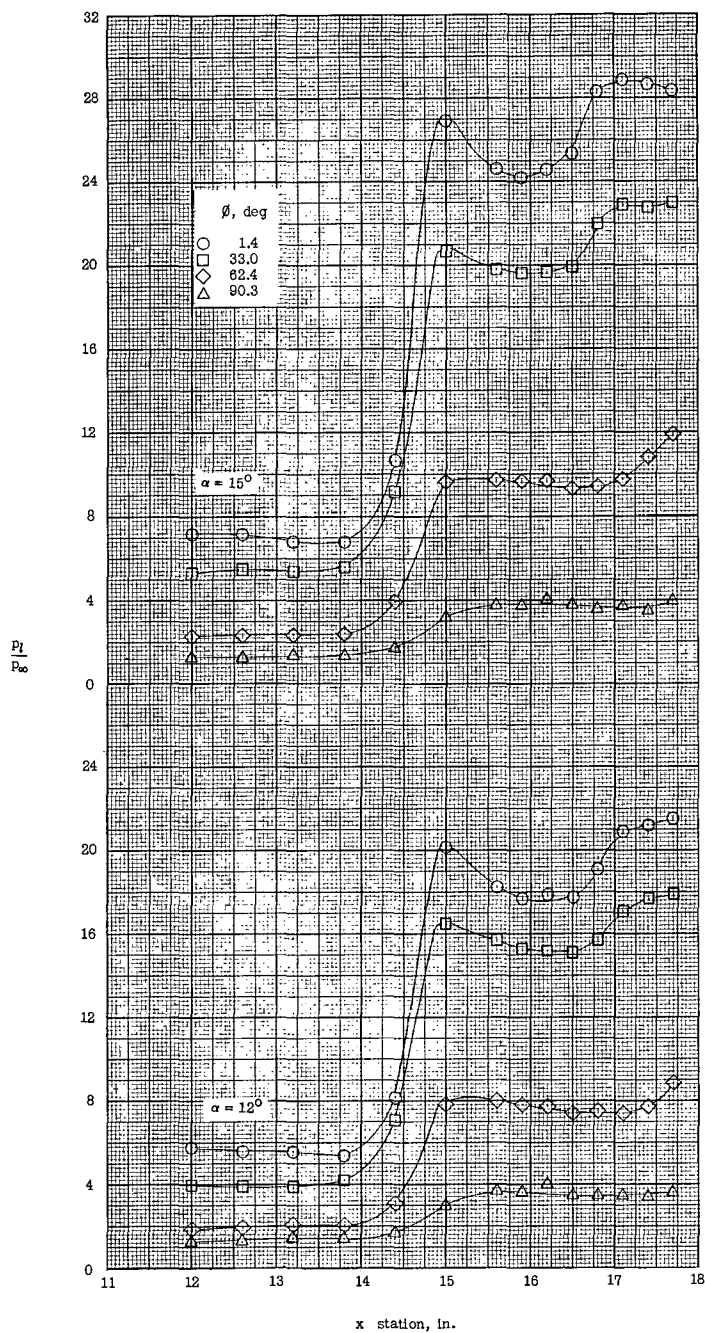


~~CONFIDENTIAL~~ $\alpha = 15^\circ$  $\alpha = 12^\circ$ 

(c) Schlieren photographs;  $\alpha = 12^\circ$  and  $15^\circ$ . L-62-4

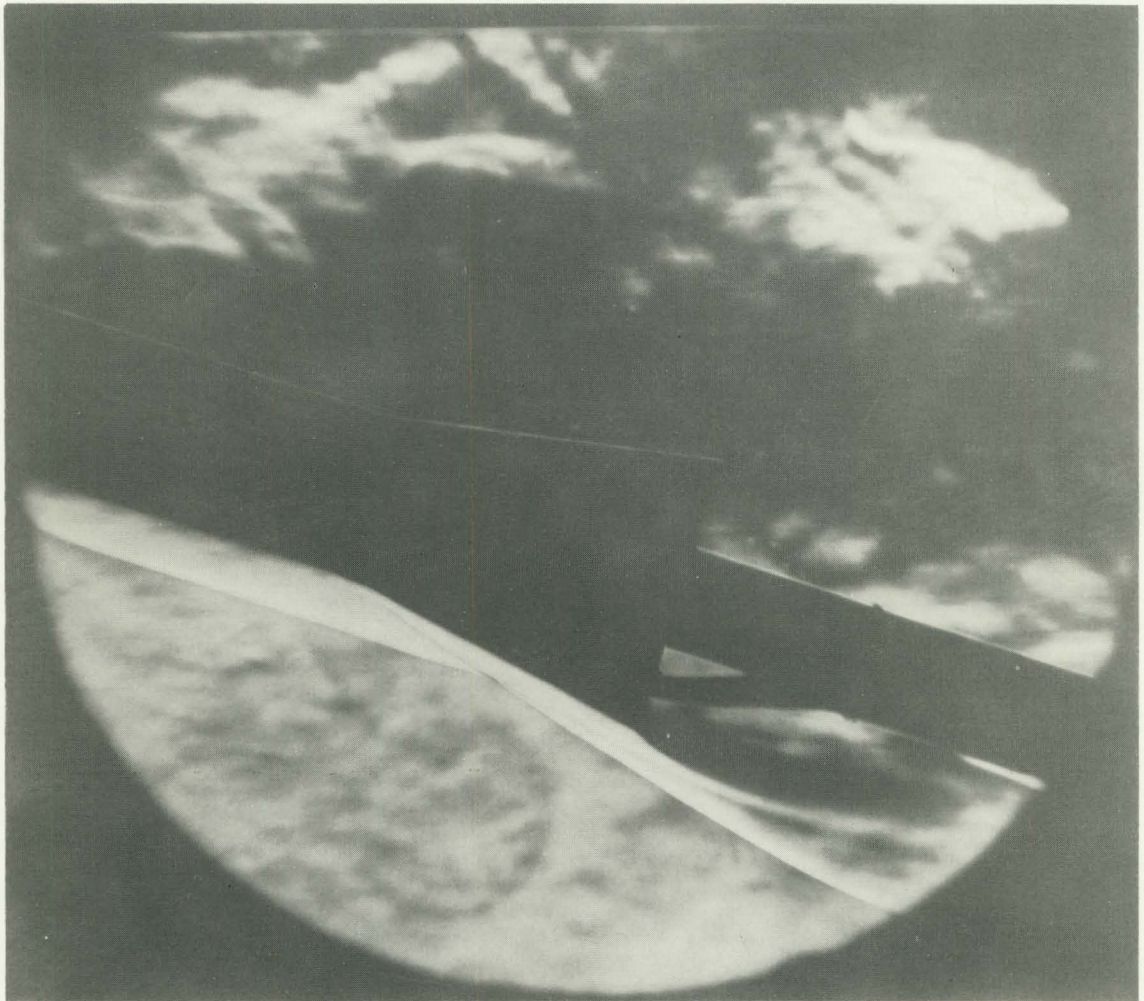
Figure 11.- Continued.

~~CONFIDENTIAL~~



(d) Pressure data;  $\alpha = 12^\circ$  and  $15^\circ$ .

Figure 11.- Continued.

~~CONFIDENTIAL~~

(e) Schlieren photograph;  $\alpha = 18^\circ$ . L-62-5

Figure 11.- Continued.

~~CONFIDENTIAL~~

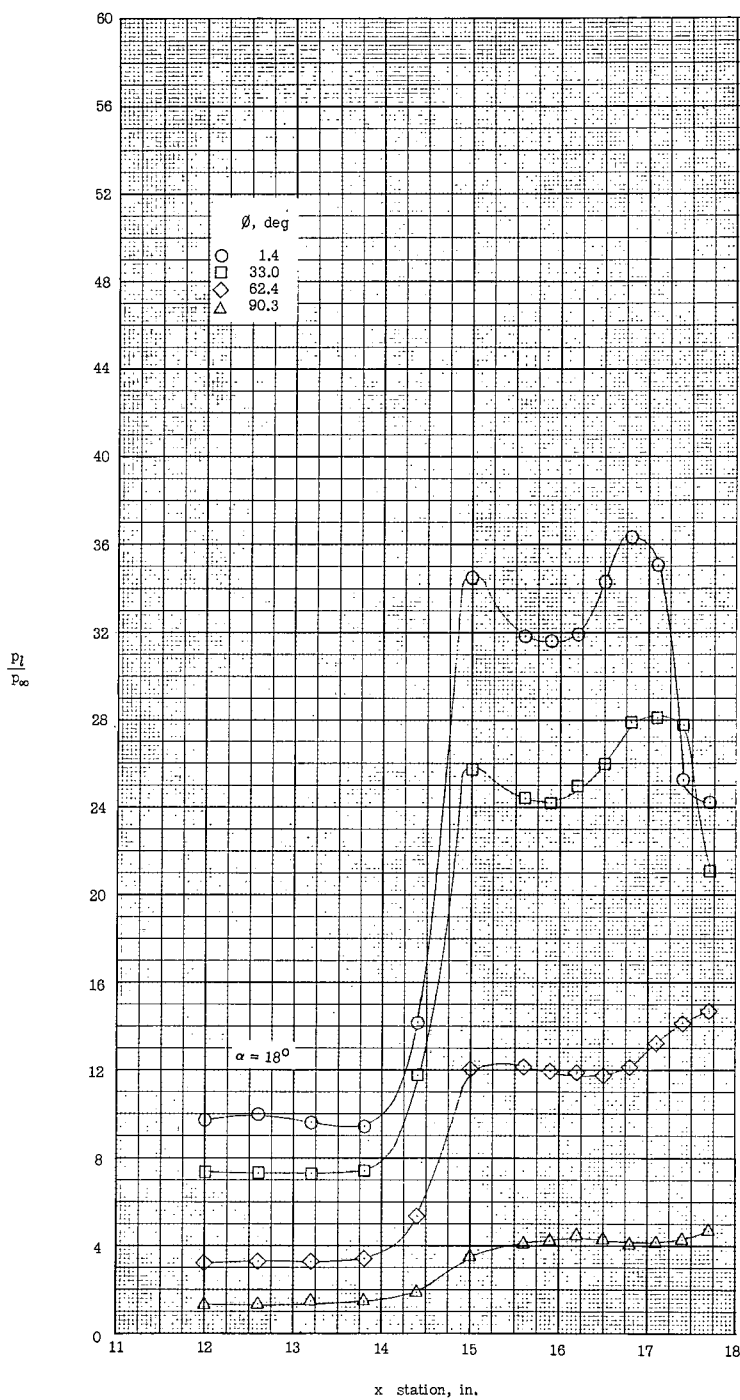
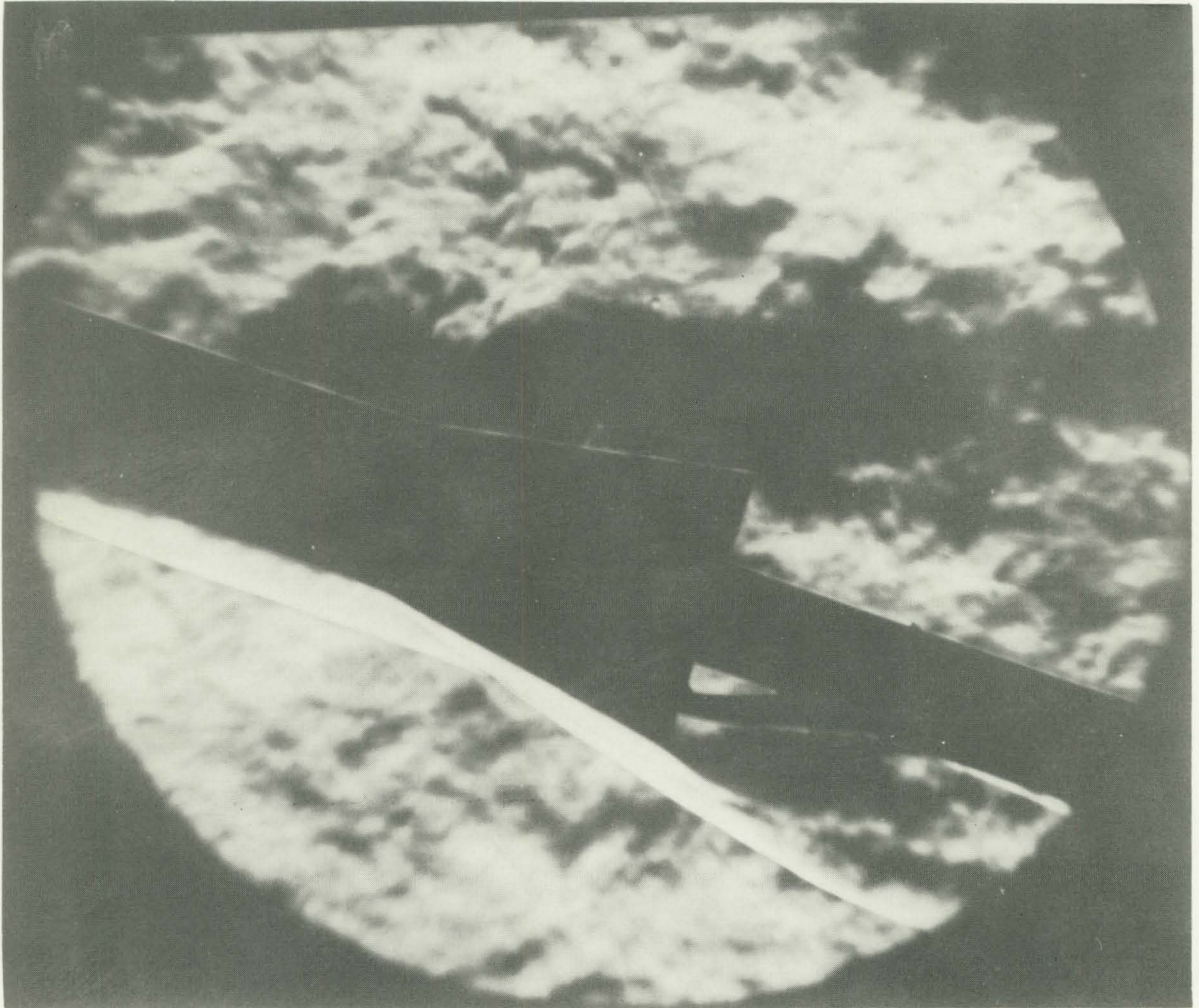
(f) Pressure data;  $\alpha = 18^\circ$ .

Figure 11.- Continued.



~~CONFIDENTIAL~~

(g) Schlieren photograph;  $\alpha = 21^\circ$ . L-62-6

Figure 11.- Continued.

~~CONFIDENTIAL~~

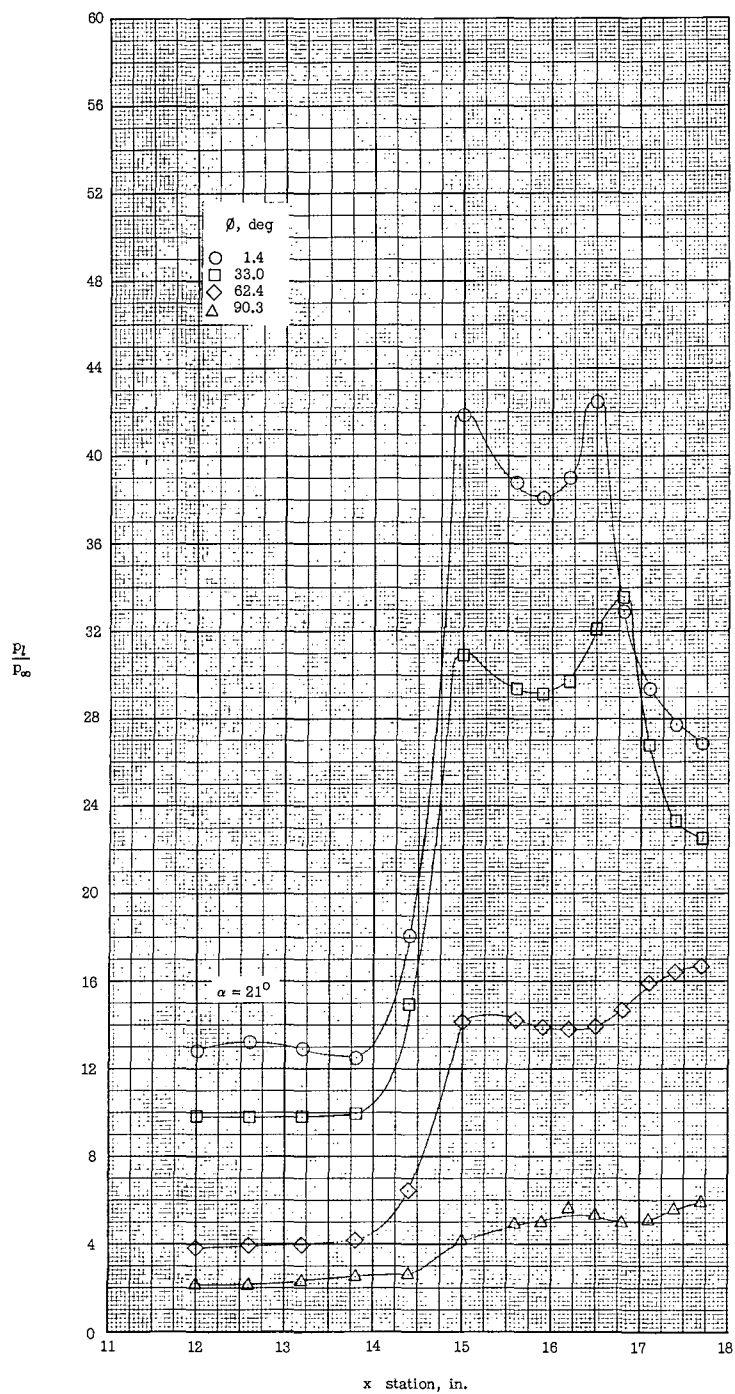
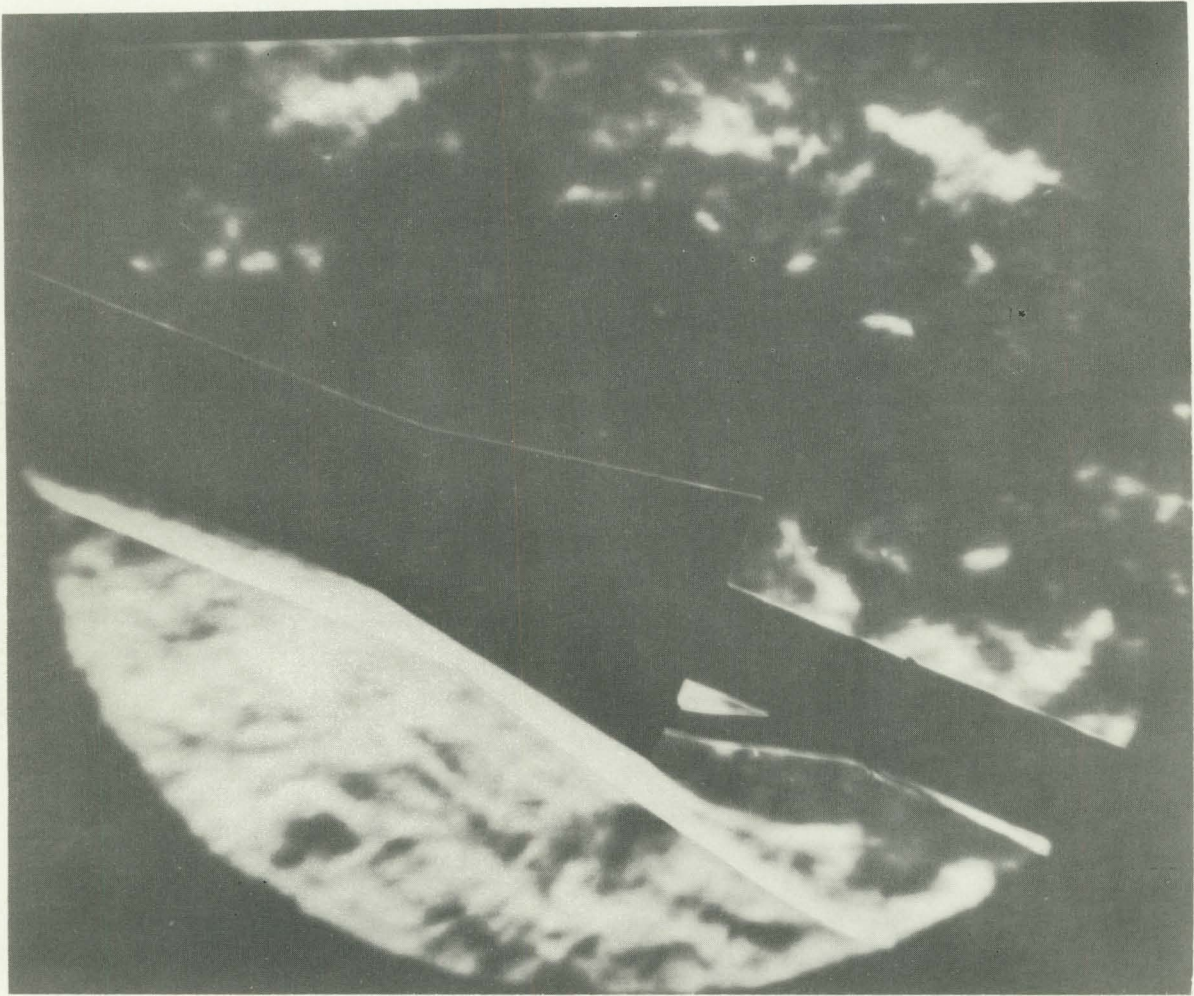
(h) Pressure data;  $\alpha = 21^\circ$ .

Figure 11.- Continued.

~~CONFIDENTIAL~~

(1) Schlieren photograph;  $\alpha = 24^\circ$ . L-62-7

Figure 11.- Continued.

~~CONFIDENTIAL~~

L-1813

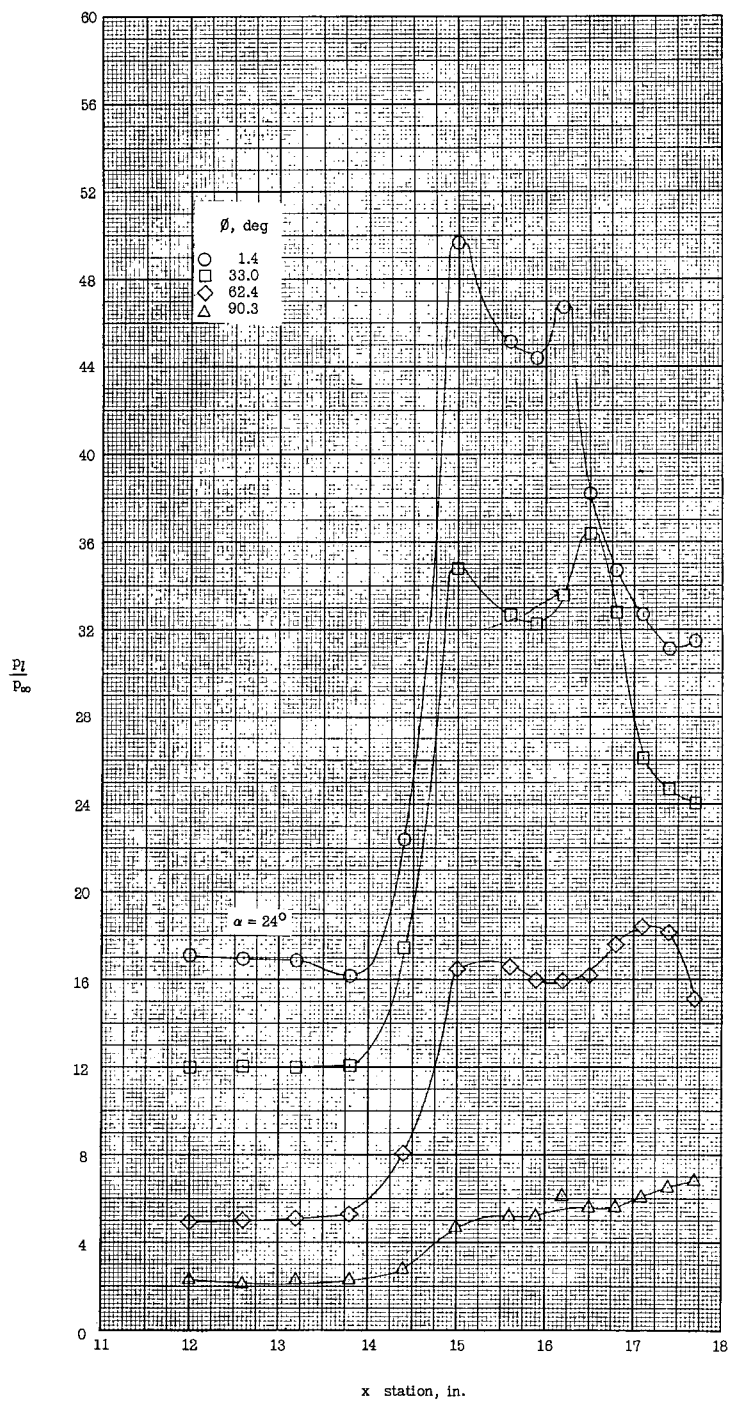
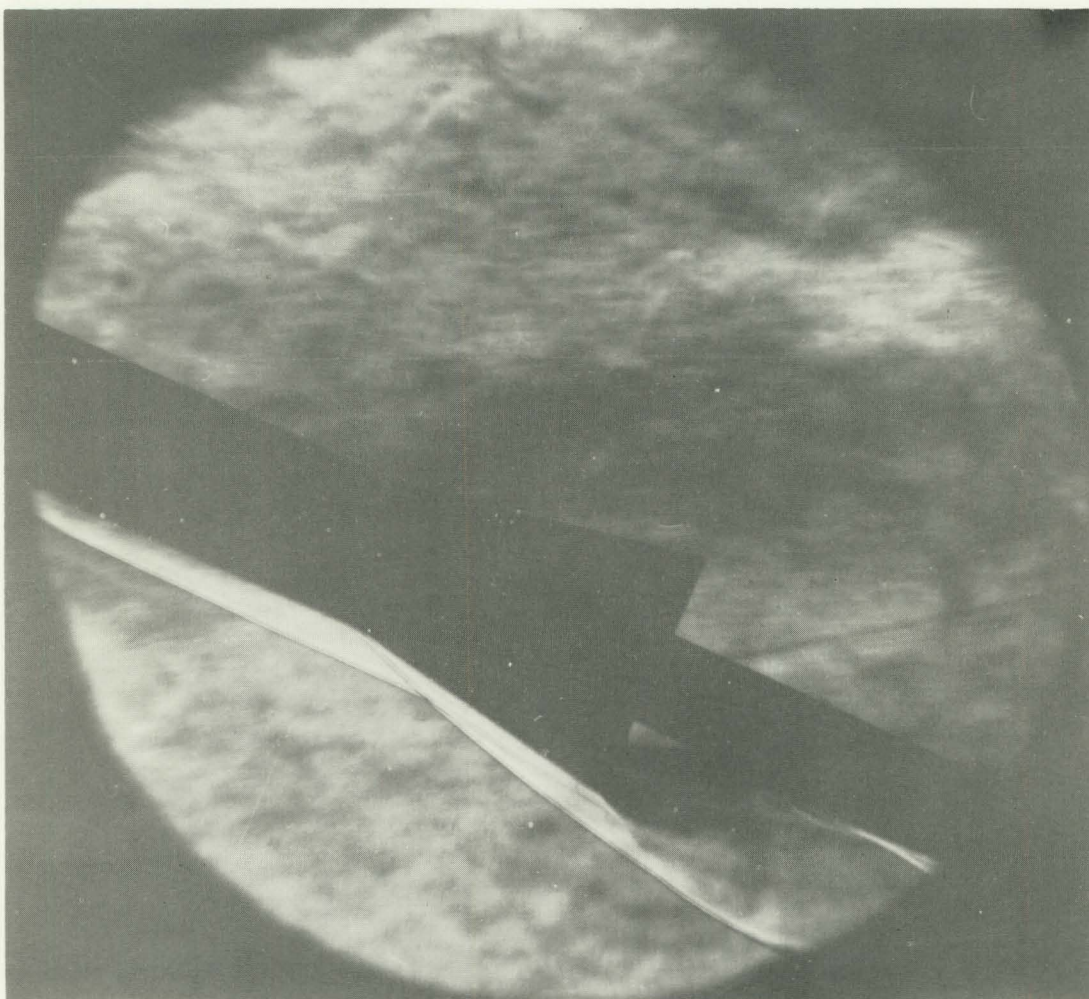
(j) Pressure data;  $\alpha = 24^\circ$ .

Figure 11.- Continued.



~~CONFIDENTIAL~~

Reproduced from  
best available copy.

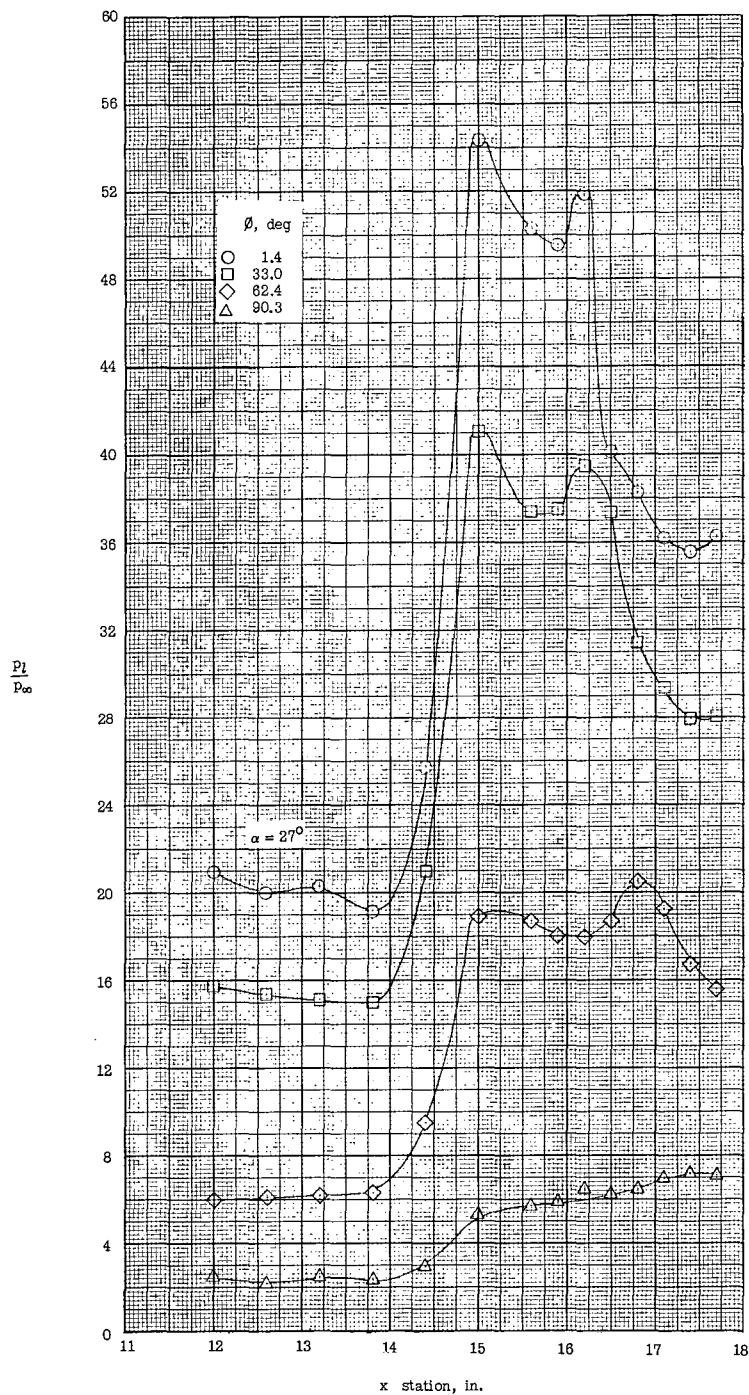


(k) Schlieren photograph;  $\alpha = 27^\circ$ . L-62-8

Figure 11.- Continued.

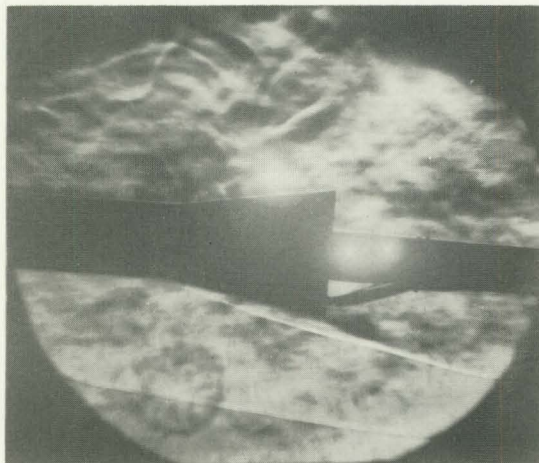
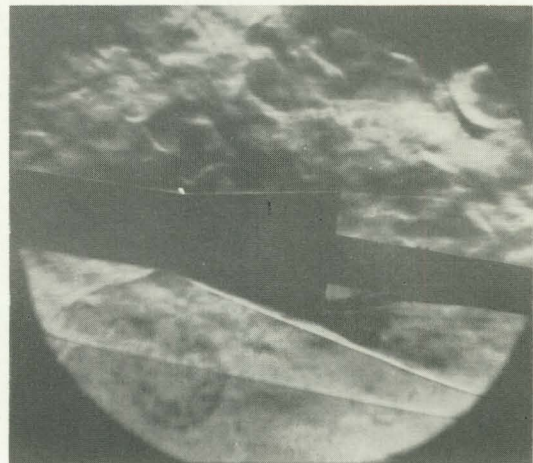
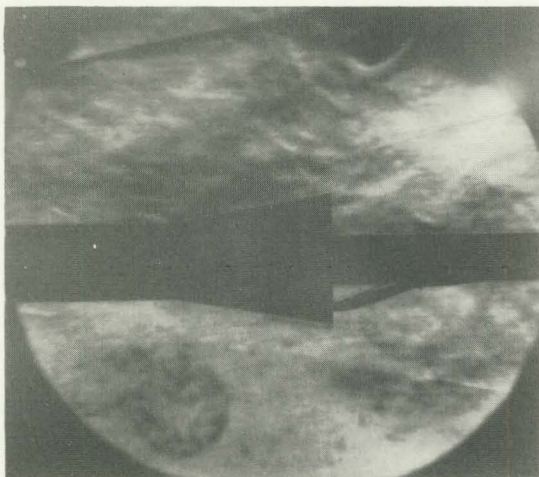
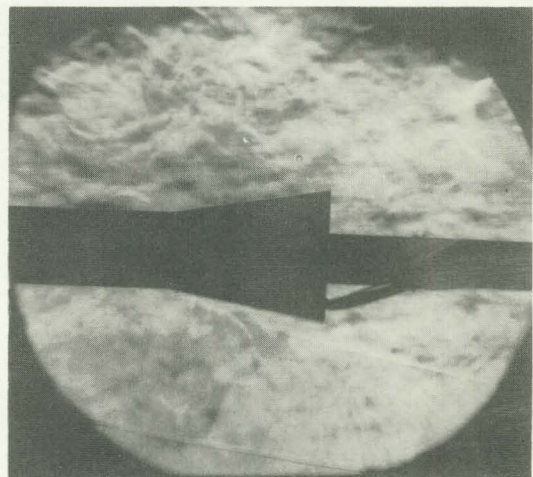
~~CONFIDENTIAL~~

L-1813



(1) Pressure data;  $\alpha = 27^\circ$ .

Figure 11.- Concluded.

~~CONFIDENTIAL~~ $\alpha = 6^\circ$  $\alpha = 9^\circ$  $\alpha = 0^\circ$  $\alpha = 3^\circ$ 

(a) Schlieren photographs;  $\alpha = 0^\circ, 3^\circ, 6^\circ$ , and  $9^\circ$ . L-62-9

Figure 12.- Schlieren photographs and pressure data on aft portion of configuration II over an angle-of-attack range from  $0^\circ$  to  $26^\circ$ .  
 $M = 8.5$ .

~~CONFIDENTIAL~~

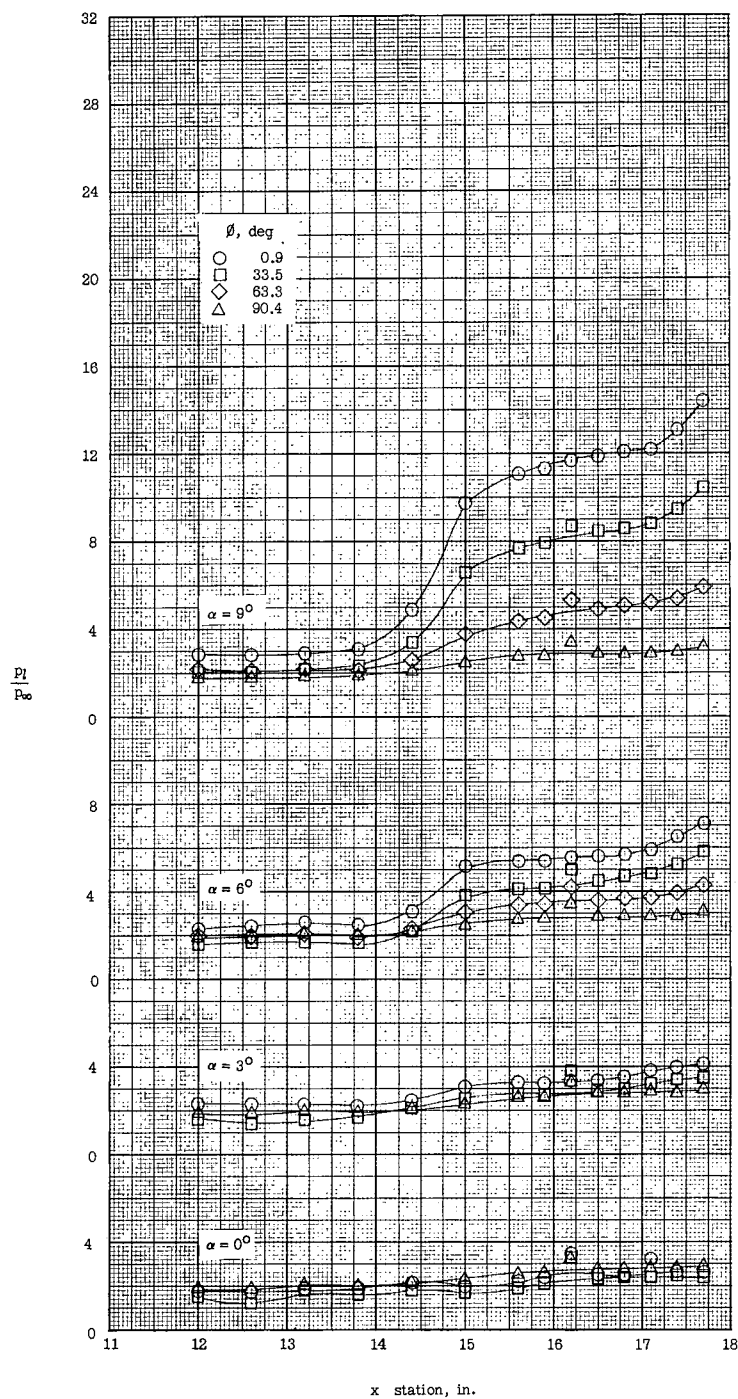
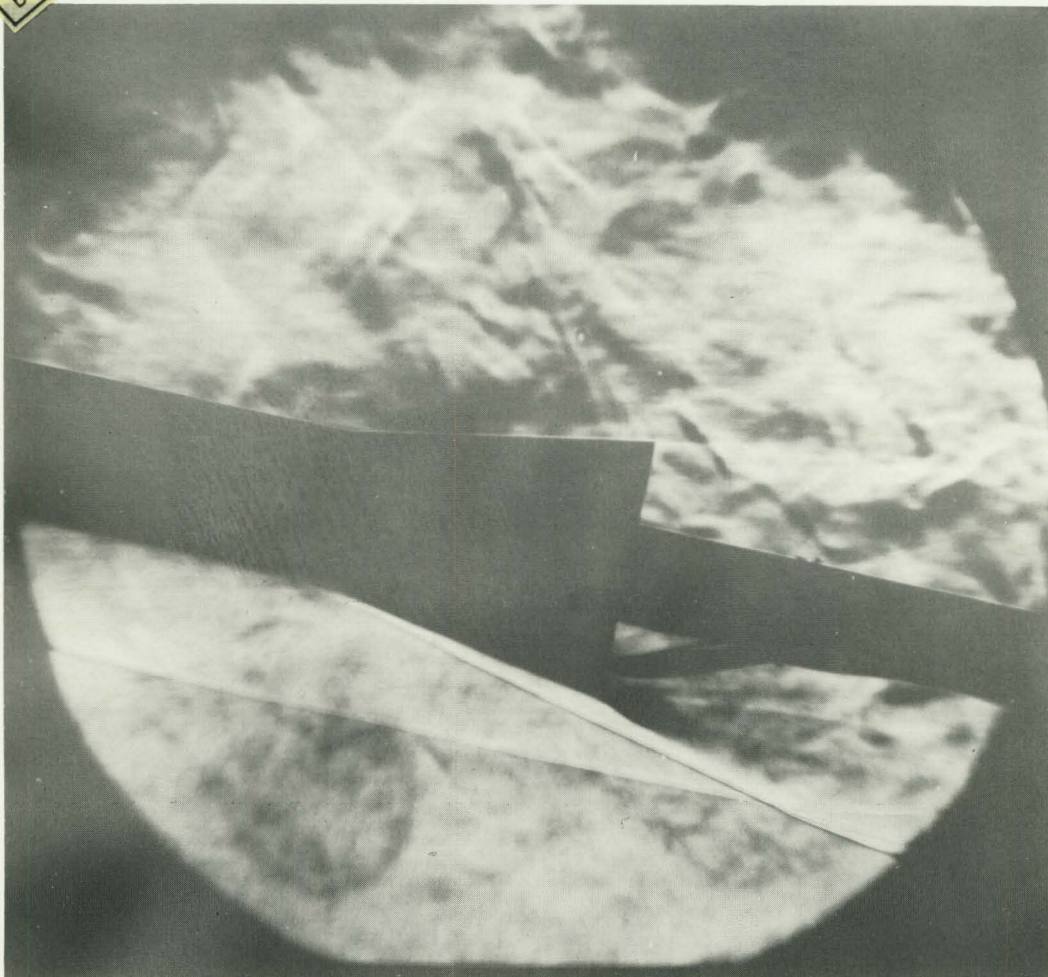
(b) Pressure data;  $\alpha = 0^\circ, 3^\circ, 6^\circ, \text{ and } 9^\circ$ .

Figure 12.- Continued.



~~CONFIDENTIAL~~

Reproduced from  
best available copy.



(c) Schlieren photograph;  $\alpha = 12^\circ$ .

L-62-10

Figure 12.- Continued.

~~CONFIDENTIAL~~

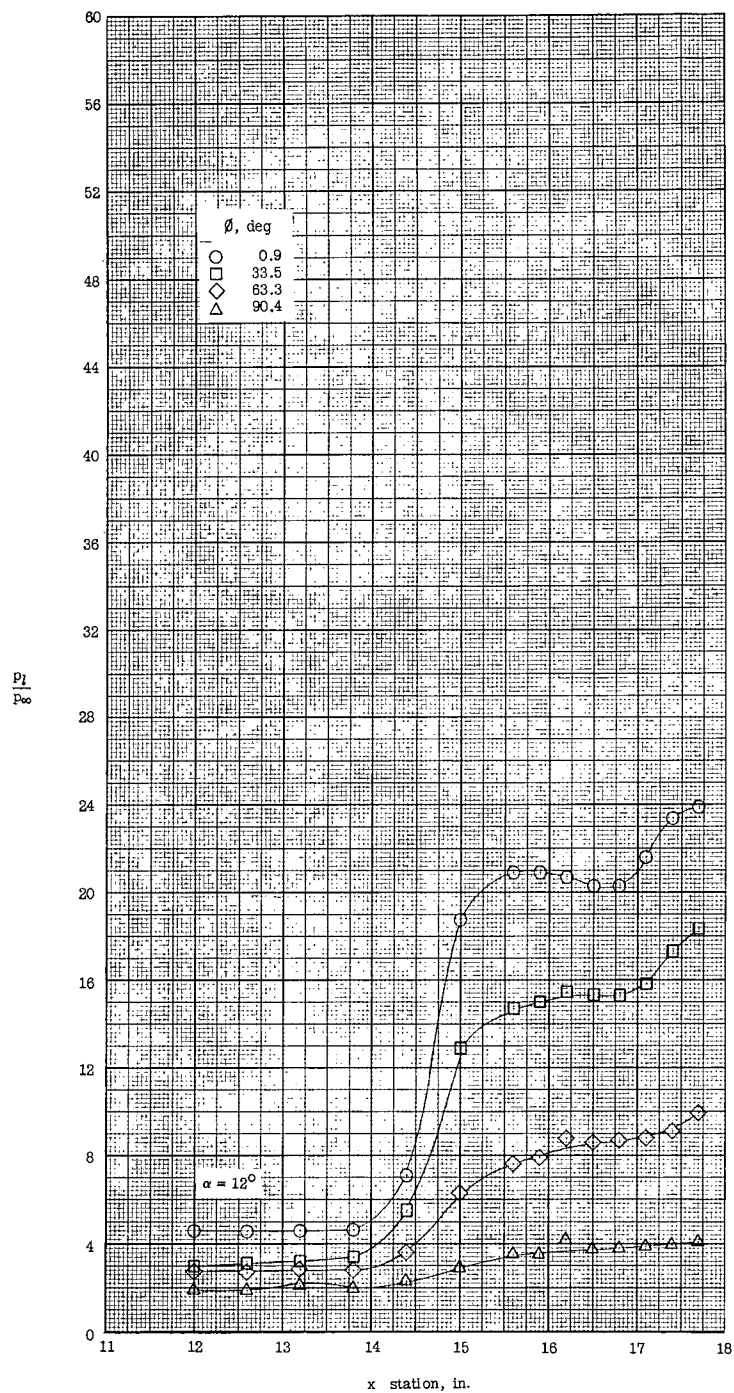
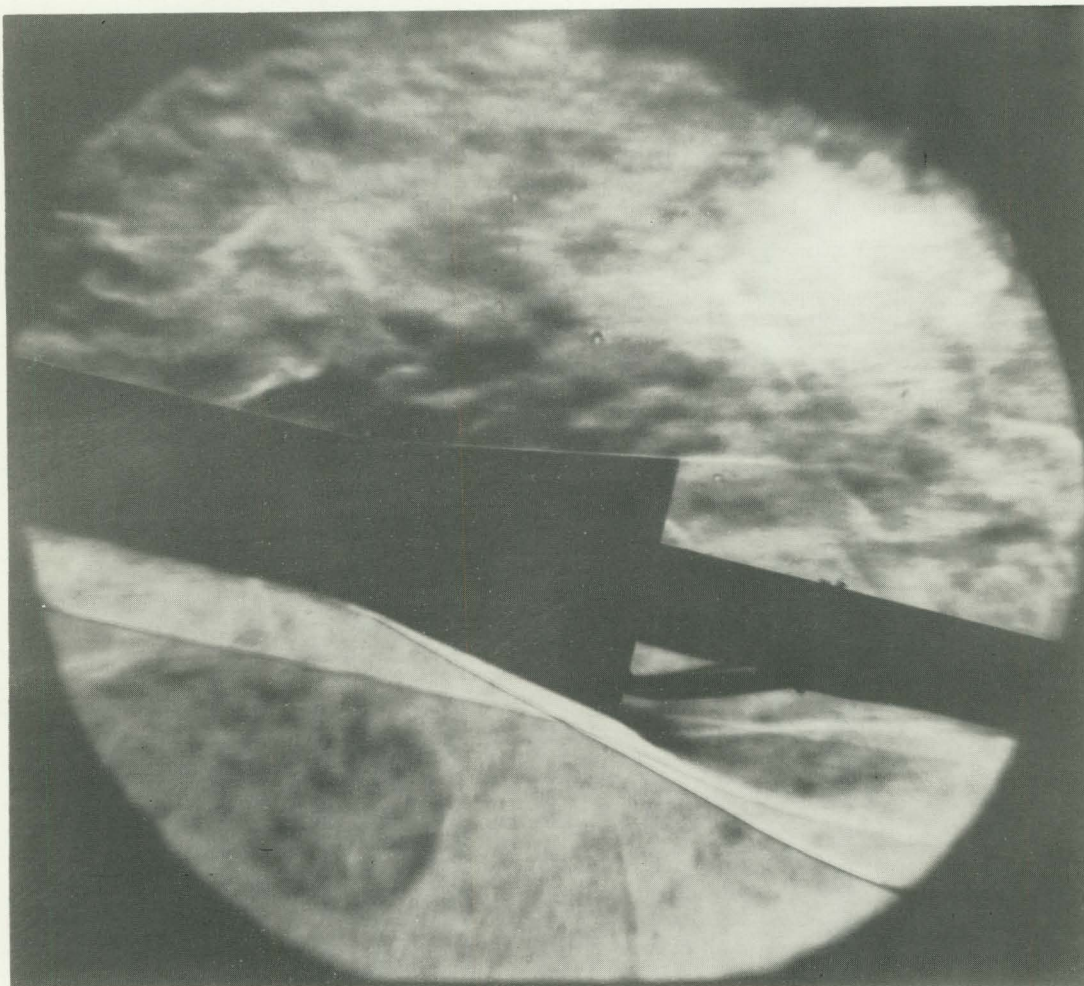
(d) Pressure data;  $\alpha = 12^\circ$ .

Figure 12.- Continued.

~~CONFIDENTIAL~~

(e) Schlieren photograph;  $\alpha = 15^\circ$ .

L-62-11

Figure 12.- Continued.

~~CONFIDENTIAL~~

L-1813

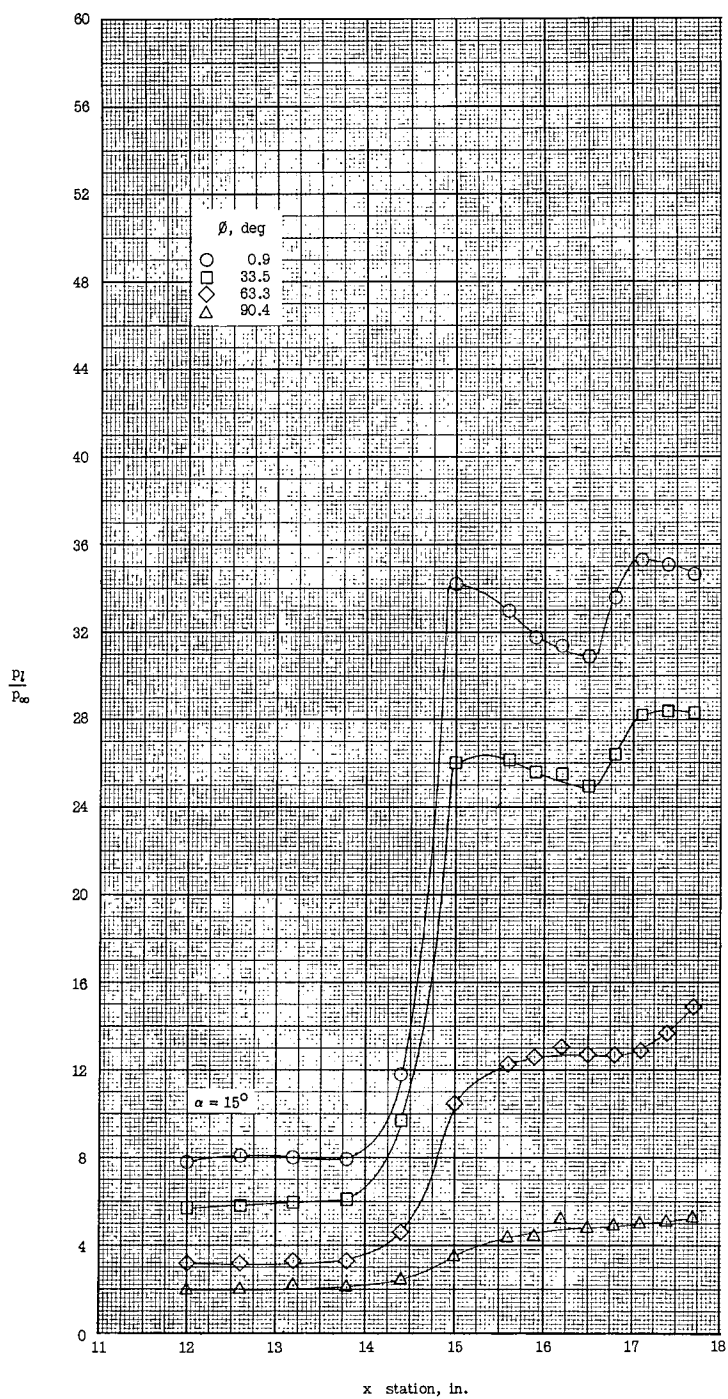
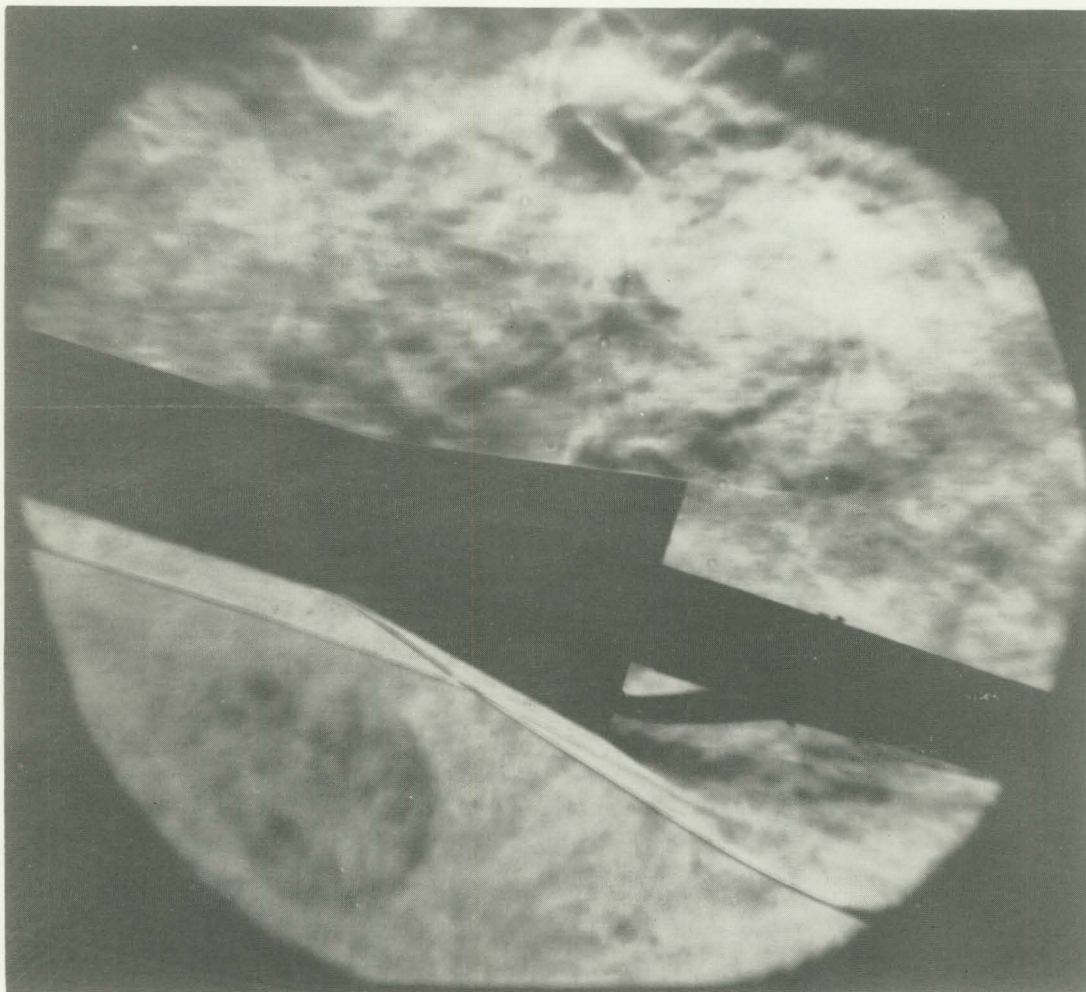
(f) Pressure data;  $\alpha = 15^\circ$ .

Figure 12.- Continued.



~~CONFIDENTIAL~~

(g) Schlieren photograph;  $\alpha = 18^\circ$ .

L-62-12

Figure 12.- Continued.

~~CONFIDENTIAL~~

L-1813

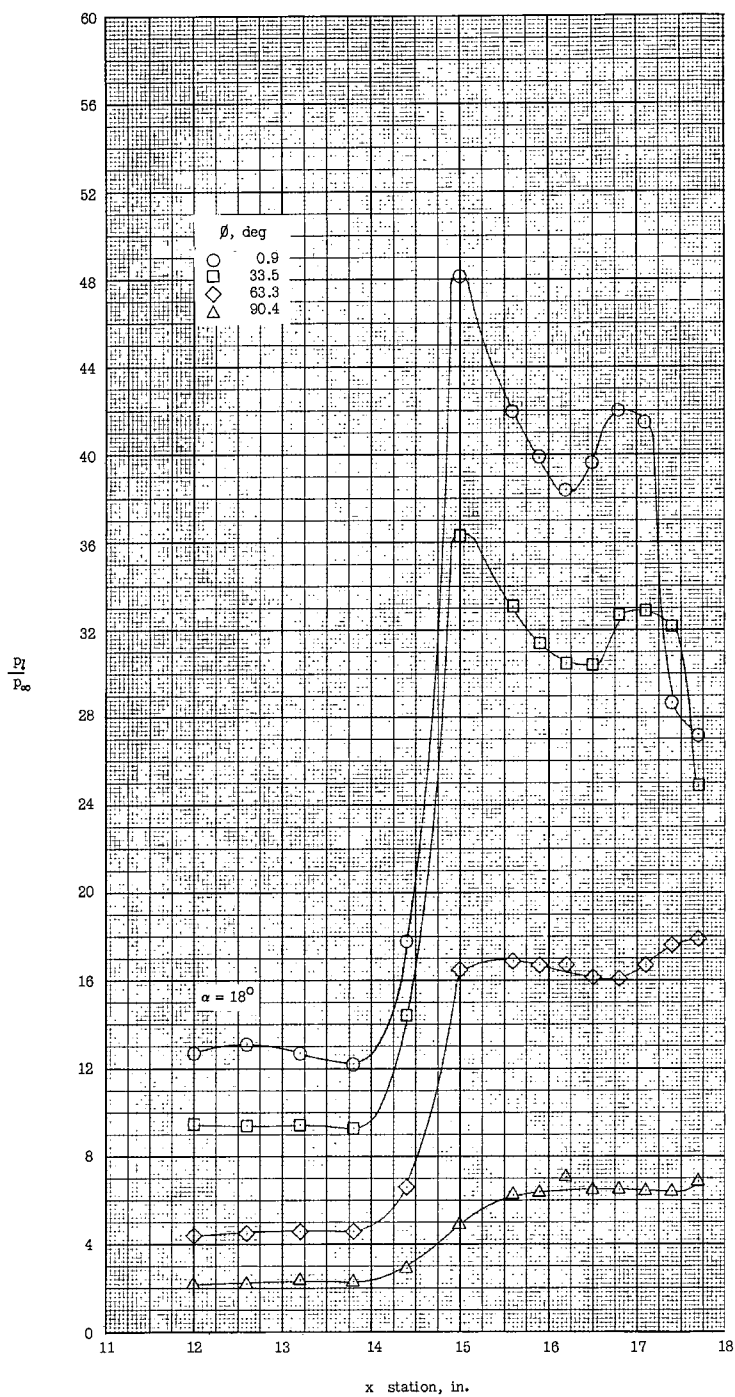
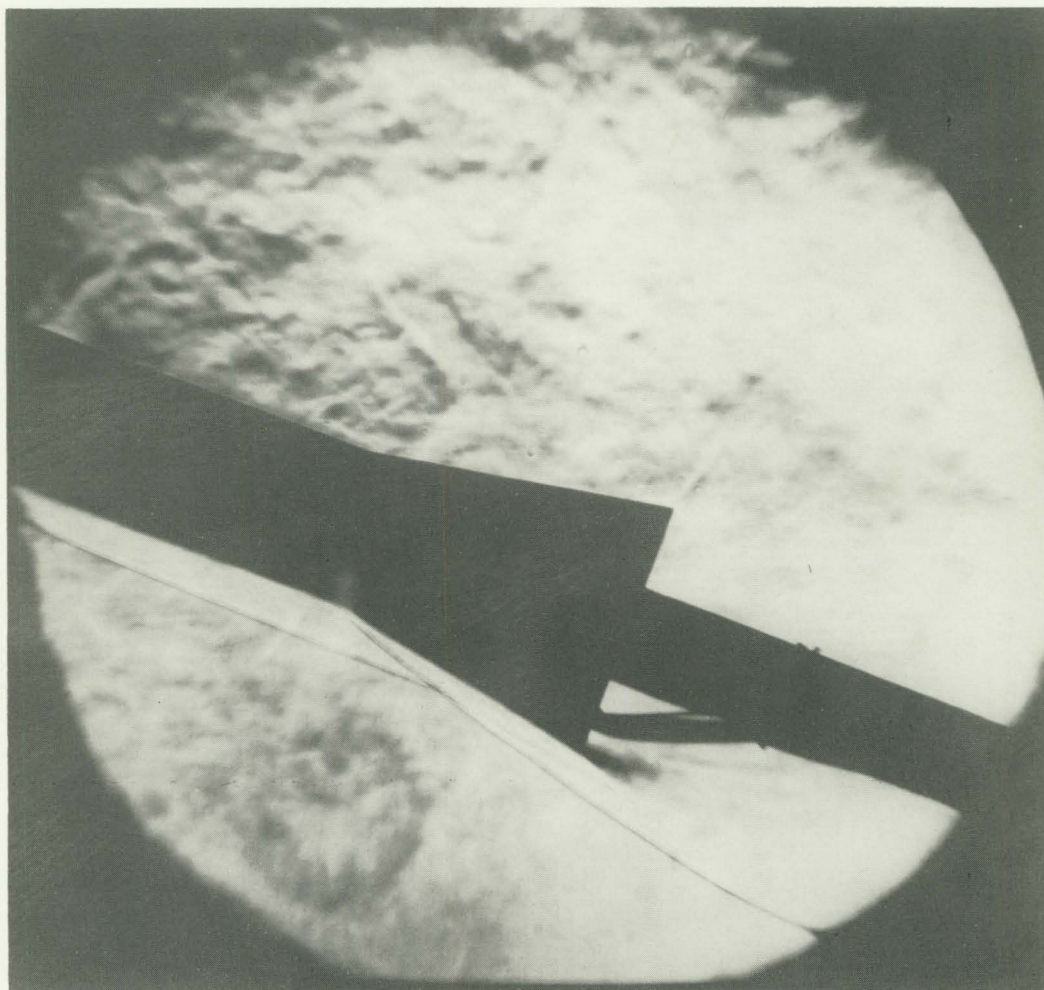
(h) Pressure data;  $\alpha = 18^\circ$ .

Figure 12.- Continued.

~~CONFIDENTIAL~~

Reproduced from  
best available copy.



(i) Schlieren photograph;  $\alpha = 21^\circ$ .

L-62-13

Figure 12.- Continued.

~~CONFIDENTIAL~~

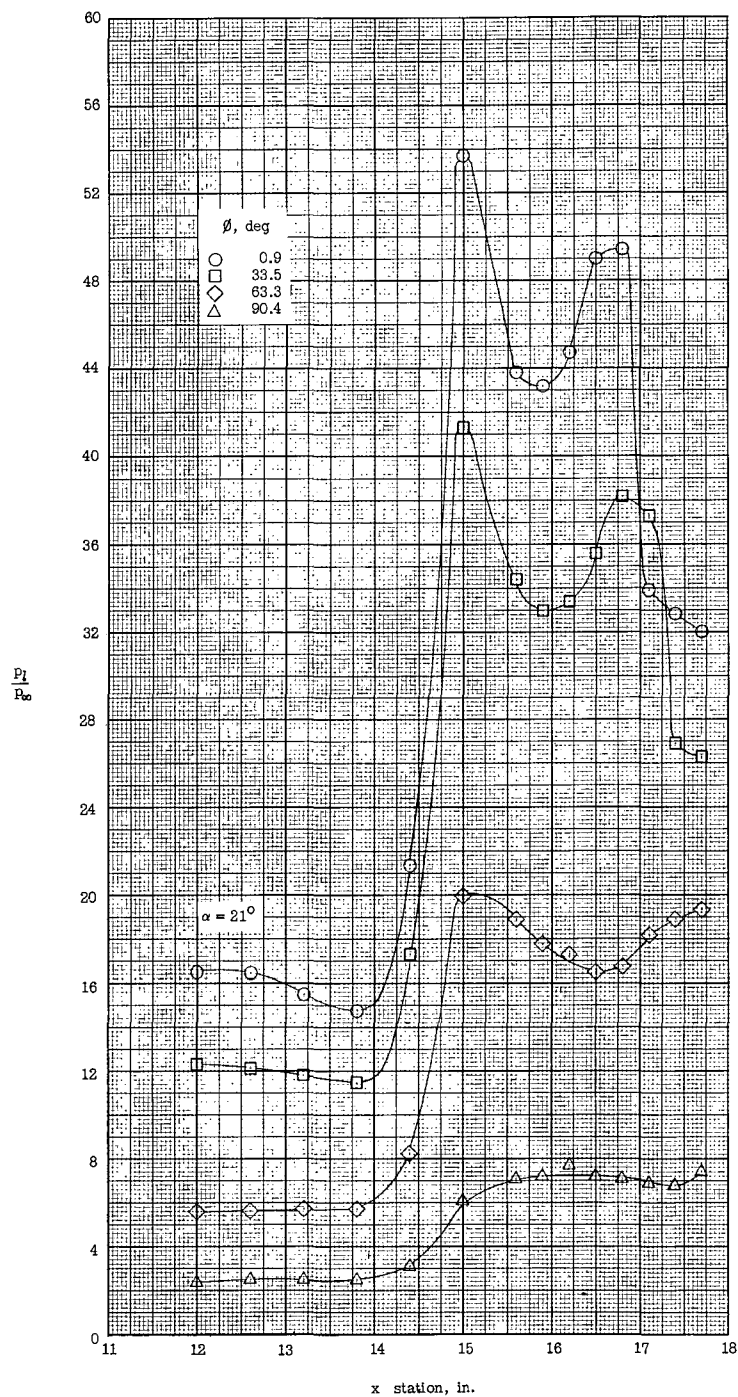
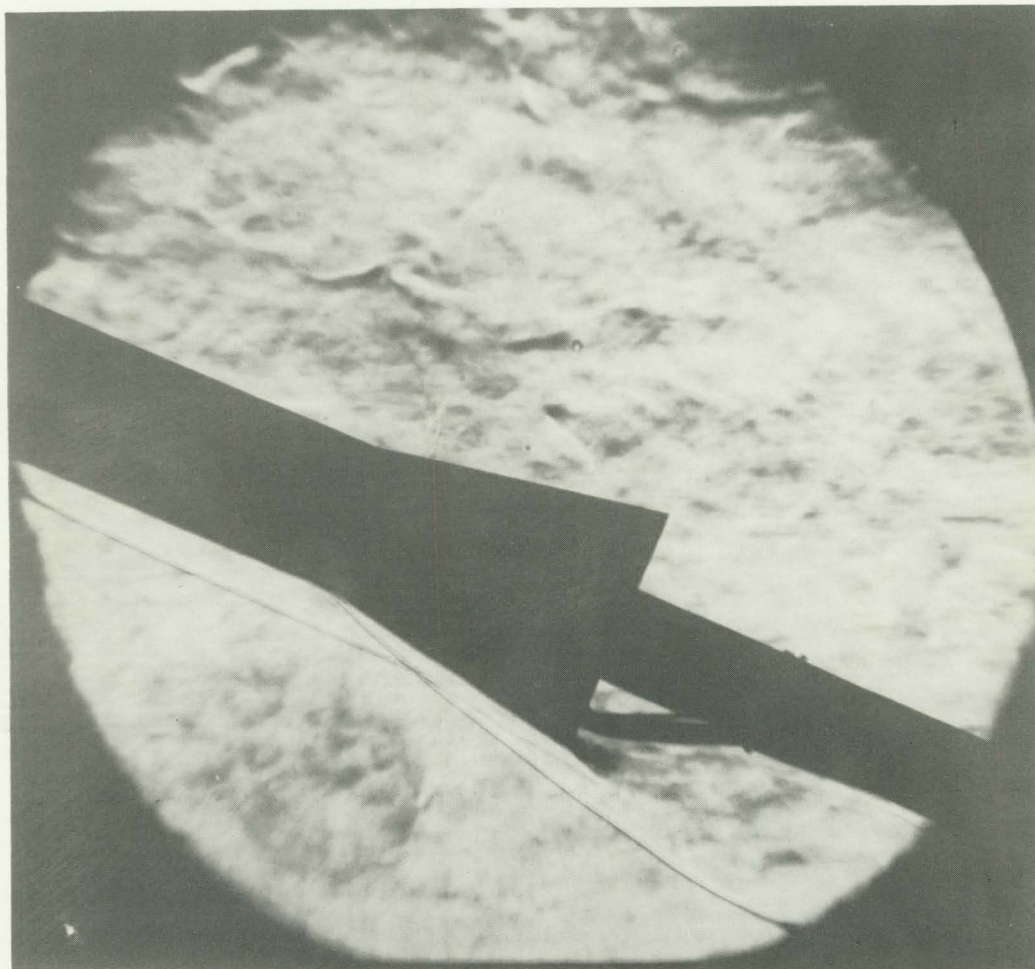
(j) Pressure data;  $\alpha = 21^\circ$ .

Figure 12.- Continued.



~~CONFIDENTIAL~~

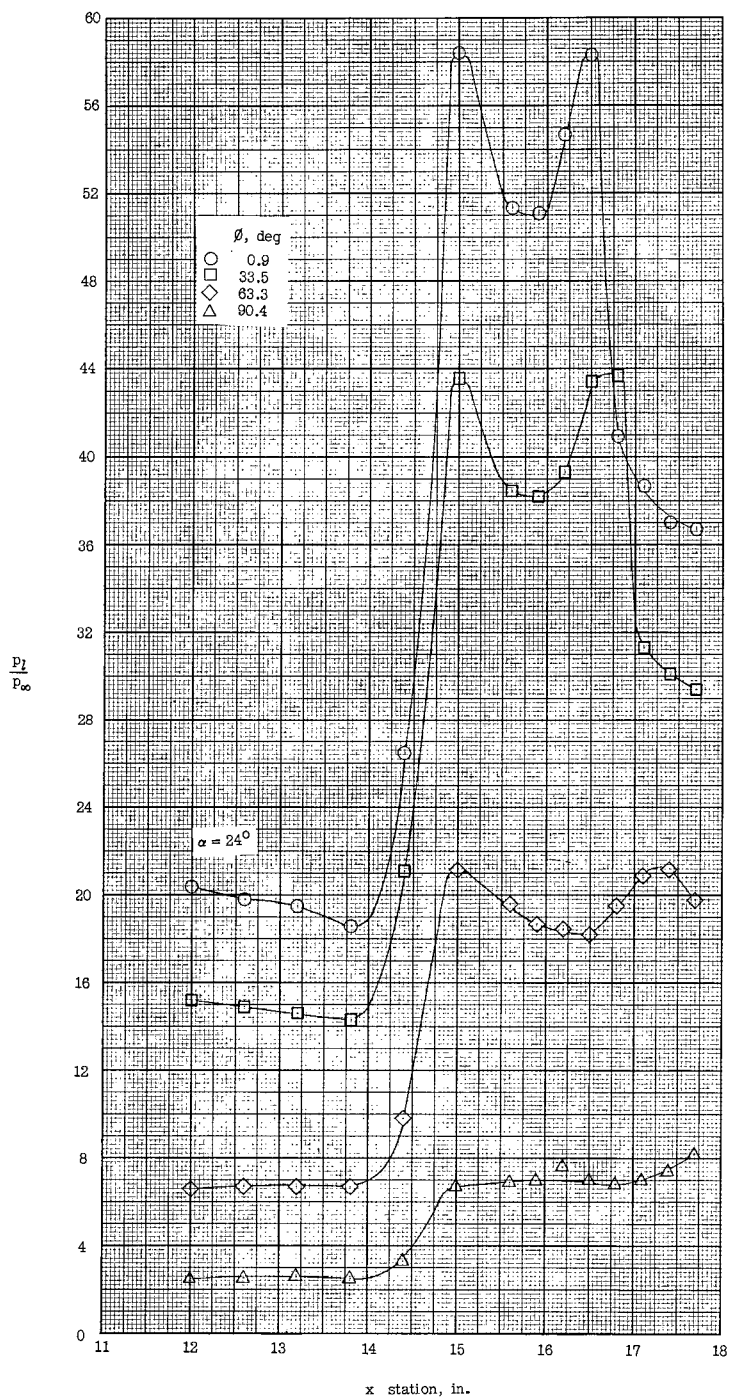
(k) Schlieren photograph;  $\alpha = 24^\circ$ .

L-62-14

Figure 12.- Continued.

~~CONFIDENTIAL~~

L-1813

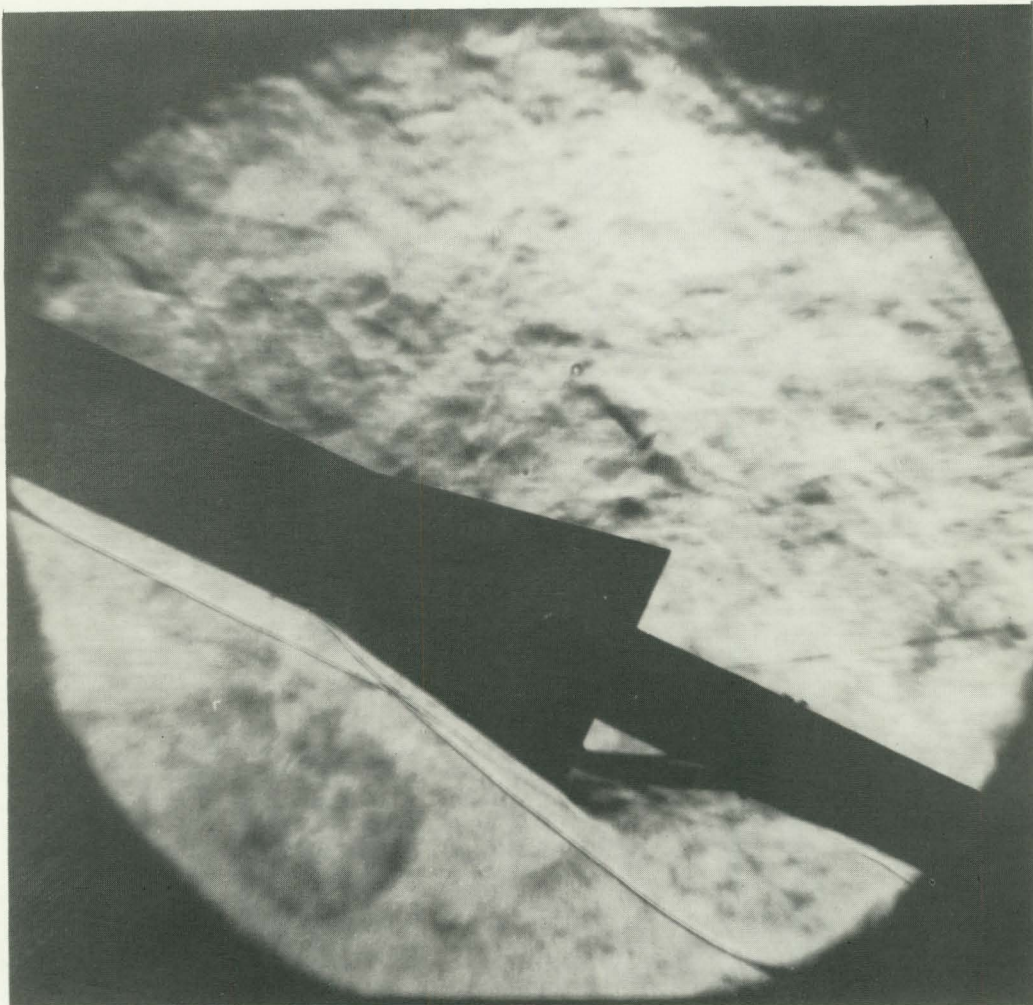


(1) Pressure data;  $\alpha = 24^\circ$ .

Figure 12.- Continued.

Reproduced from  
best available copy.

~~CONFIDENTIAL~~



(m) Schlieren photograph;  $\alpha = 26^\circ$ .

L-62-15

Figure 12.- Continued.

~~CONFIDENTIAL~~

L-1813

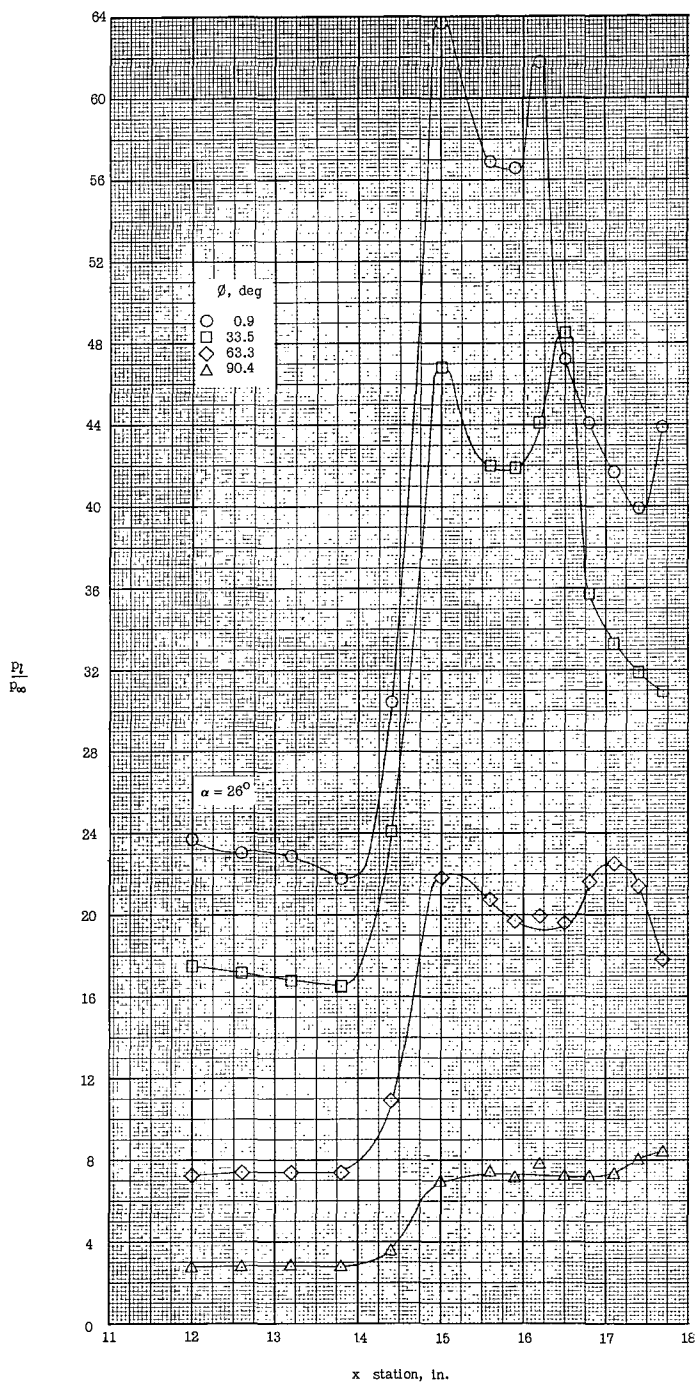
(n) Pressure data;  $\alpha = 26^\circ$ .

Figure 12.- Concluded.



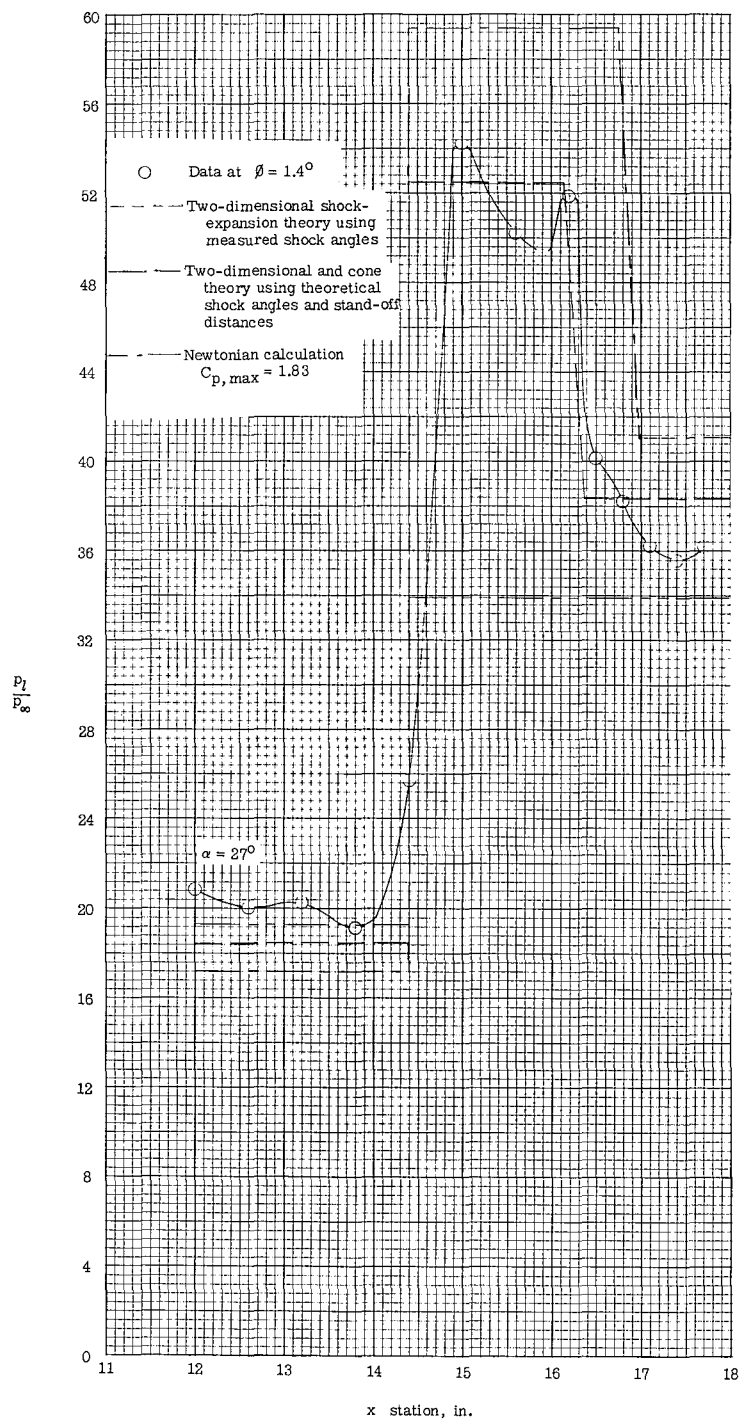


Figure 13.- Theoretical approximations of pressures on the  $0^\circ$  meridian of configuration I at  $\alpha = 27^\circ$ .  $M = 8.5$ .

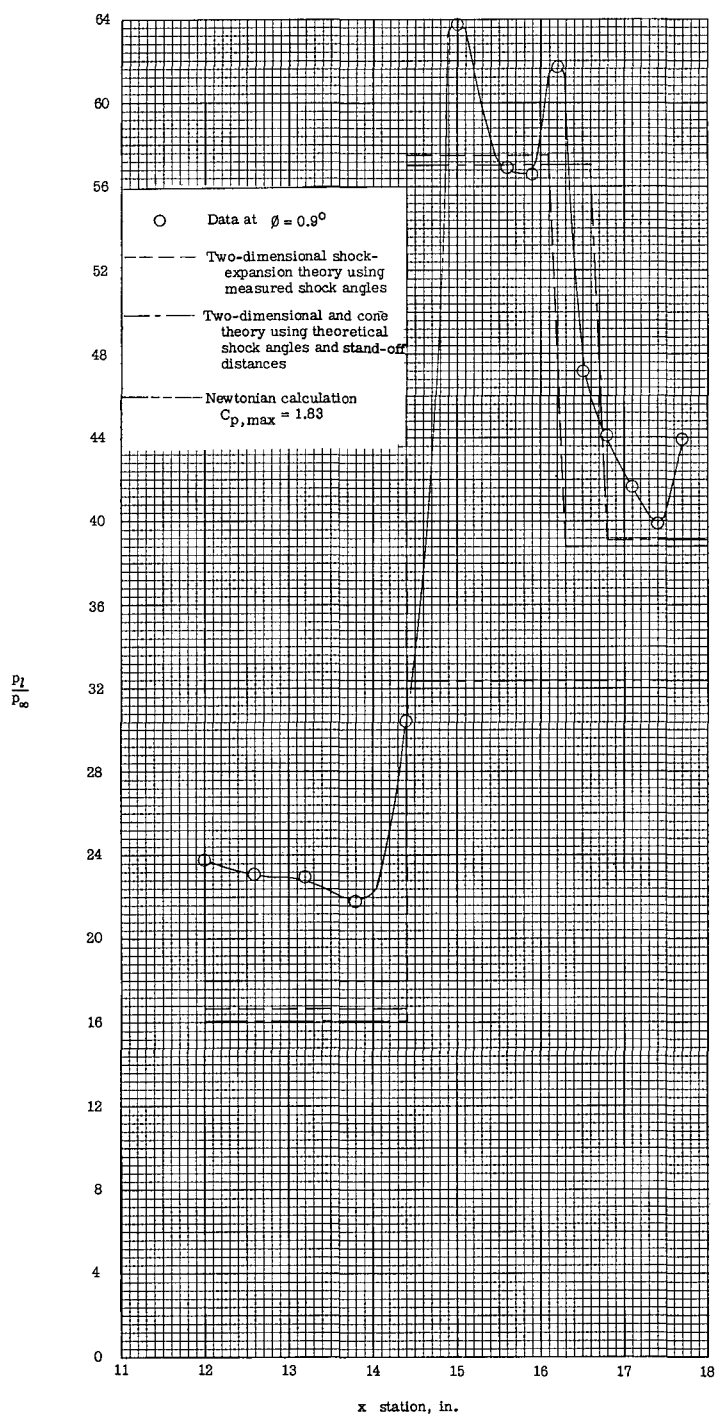


Figure 14.- Theoretical approximations of pressures on the  $0^\circ$  meridian of configuration II at  $\alpha = 26^\circ$ .  $M = 8.5$ .